

A VERY DEEP *CHANDRA* OBSERVATION OF ABELL 2052: BUBBLES, SHOCKS, AND SLOSHING

E. L. BLANTON^{1,2}, S. W. RANDALL², T. E. CLARKE³, C. L. SARAZIN⁴, B. R. MCNAMARA^{5,2,6}, E. M. DOUGLASS¹, AND M. McDONALD⁷

Accepted for publication in ApJ

ABSTRACT

We present first results from a very deep (~ 650 ksec) *Chandra* X-ray observation of Abell 2052, as well as archival VLA radio observations. The data reveal detailed structure in the inner parts of the cluster, including bubbles evacuated by the AGN’s radio lobes, compressed bubble rims, filaments, and loops. Two concentric shocks are seen, and a temperature rise is measured for the innermost one. On larger scales, we report the first detection of an excess surface brightness spiral feature. The spiral has cooler temperatures, lower entropies, and higher abundances than its surroundings, and is likely the result of sloshing gas initiated by a previous cluster-cluster or sub-cluster merger. Initial evidence for previously unseen bubbles at larger radii related to earlier outbursts from the AGN is presented.

Subject headings: galaxies: clusters: general — cooling flows — intergalactic medium — radio continuum: galaxies — X-rays: galaxies: clusters — galaxies: clusters: individual(A2052)

1. INTRODUCTION

With its sub-arcsec resolution, the *Chandra* X-ray Observatory has revealed a wealth of substructure in the X-ray-emitting intracluster medium (ICM) in clusters of galaxies. “Cavities” or “bubbles” are commonly seen in the X-ray gas in cluster centers related to outbursts by the active galactic nucleus (AGN). In addition, surface brightness edges associated with shocks and cold fronts have been observed, as well as spiral features likely related to “sloshing” of the intracluster medium in cluster centers.

The central bubbles are frequently seen in cooling flow (or “cool core”) clusters and are often filled with radio emission associated with the AGN. There was some evidence for these features in a very few cases even before *Chandra* observations (e.g. *ROSAT* observations of Perseus [Böhringer et al. 1993], Abell 4059 [Huang & Sarazin 1998], and Abell 2052 [Rizza et al. 2000]). Clusters with cool cores have radio bubbles much more often than non-cool core clusters (e.g. Mittal et al. 2009), and some of the most spectacular individual cases observed by *Chandra* are the Perseus cluster (Fabian et al. 2003, 2006), M87/Virgo (Forman et al. 2005, 2007), Hydra A (McNamara et al. 2000, Wise et al. 2007), MS0735.6+7421 (McNamara et al. 2005), and Abell 2052 (Blanton et al. 2001, 2003, 2009, 2010).

The classic “cooling flow problem” is that sufficient

quantities of cool gas (as evidenced by star formation rates, for example) were not found to match the gas cooling rates estimated from earlier X-ray observatories. The X-ray cooling rates have lowered based on *Chandra* and *XMM-Newton* observations, and the majority of the gas is seen to cool to only some fraction (typically one-third to one-half) of the cluster average temperature (Peterson et al. 2003). A heating mechanism is required to stop the gas from cooling to even lower temperatures.

The most likely candidate for heating of the central cluster gas is feedback from central AGN that are fed by the cooling gas (see McNamara & Nulsen 2007 for a review). This heating comes in the form of bubbles inflated by the AGN, described above, that then rise buoyantly to larger radii in cluster atmospheres distributing the heat. The details of this heating, however, are still not completely understood. In addition, there is at least some component of shock heating in many cluster centers, especially early on in the AGN’s lifetime. Shocks have been detected in fewer cases than radio bubbles, and observations include those of Perseus (Fabian et al. 2003, 2006; Graham et al. 2008), M87/Virgo (Forman et al. 2005), Hydra A (Nulsen et al. 2005a), Hercules A (Nulsen et al. 2005b), MS0735.6+7421 (McNamara et al. 2005), and the group NGC 5813 (Randall et al. 2011). Typically, the shocks are weak with Mach numbers ranging from approximately 1.2 to 1.7 (McNamara & Nulsen 2007). In even fewer cases are temperature rises detected associated with the shocks.

Heating of the ICM may also result from gas “sloshing” in the cluster’s central potential well (Ascasibar & Markevitch 2006; ZuHone et al. 2010). Cold fronts, regions where the surface brightness changes sharply but the pressure does not, can result from these sloshing motions driven initially by cluster or sub-cluster mergers. The sloshing can produce a spiral distribution of cool cluster gas reaching into the cluster center (e.g. Clarke et al. 2004, Laganá et al. 2010), and is also seen in galaxy groups (Randall et al. 2009a).

Here, we present a very deep *Chandra* observation of the cool core cluster Abell 2052. The only other cool core

¹ Institute for Astrophysical Research and Astronomy Department, Boston University, 725 Commonwealth Avenue, Boston, MA 02215; eblanton@bu.edu, emdoug@bu.edu

² Harvard Smithsonian Center for Astrophysics, 60 Garden Street, Cambridge, MA 02138; srandall@head.cfa.harvard.edu; ELB as Visiting Scientist

³ Naval Research Laboratory, 4555 Overlook Avenue SW, Washington D. C. 20375; tracy.clarke@nrl.navy.mil

⁴ Department of Astronomy, University of Virginia, P. O. Box 400325, Charlottesville, VA 22904-4325; sarazin@virginia.edu

⁵ Department of Physics and Astronomy, University of Waterloo, Waterloo, ON N2L 2G1, Canada; mcnamara@sciborg.uwaterloo.ca

⁶ Perimeter Institute for Theoretical Physics, 31 Caroline St., N. Waterloo, Ontario, Canada, N2L 2Y5

⁷ Astronomy Department, University of Maryland, College Park, MD 20742; mcdonald@astro.umd.edu

clusters observed to similar or greater depth with *Chandra* are Perseus (Fabian et al. 2006) and M87/Virgo (Million et al. 2010, Werner et al. 2010). Abell 2052 is a moderately rich cluster at a redshift of $z = 0.03549$ (Oegerle & Hill 2001). Its central radio source, 3C 317, is hosted by the central cD galaxy, UGC 09799. Abell 2052 was previously observed in the X-ray with *Einstein* (White, Jones, & Forman 1997), *ROSAT* (Peres et al. 1998, Rizza et al. 2000), *ASCA* (White 2000), *Chandra* (Blanton et al. 2001, 2003, 2009, 2010), *Suzaku* (Tamura et al. 2008), and *XMM-Newton* (de Plaa et al. 2010). In addition, we present archival radio observations from the Very Large Array (VLA).

We assume $H_0 = 70 \text{ km s}^{-1} \text{ Mpc}^{-1}$, $\Omega_M = 0.3$, and $\Omega_\Lambda = 0.7$ ($1'' = 0.7059 \text{ kpc}$ at $z = 0.03549$) throughout. Errors are given at the 1σ level unless otherwise stated.

2. CHANDRA OBSERVATIONS AND DATA REDUCTION

Abell 2052 was observed with *Chandra* for a total of 662 ksec in Cycles 1, 6, and 10 from 2000 – 2009. A summary of the observations is given in Table 1. All observations were performed with the ACIS-S as the primary instrument. The ACIS-S was chosen for its greater response at low energies than the ACIS-I, yielding a higher count rate for this relatively cool, $kT \approx 3 \text{ keV}$ cluster. The nominal roll angles used for the observations varied from 99° to 265° providing coverage at large radii at a range of azimuthal angles around the cluster. The events were telemetered in Very Faint mode for all but the Cycle 1 observation, where the events were telemetered in Faint mode. The data were processed in the standard manner, using CIAO 4.2 and CALDB 4.2.2. After cleaning, and filtering for background flares (using the 2.5 – 7.0 keV range for the BI chips and the 0.3 – 12.0 keV range for the FI chips), the total exposure remaining for the eleven data sets was 657 ksec. Background corrections were made using the blank-sky background fields, including the new “period E” background files for the more recent data. For each target events file, a corresponding background events file was created, normalizing by the ratio of counts in the 10 – 12 keV energy range for the source and background files to set the scaling.

3. RADIO DATA

We have used the NRAO data archive to extract observations of 3C 317 at 4.8 and 1.4 GHz. A summary of the data sets is presented in Table 2. The archival radio data were calibrated and reduced with the NRAO Astronomical Image Processing System (AIPS). Images were produced through the standard Fourier transform deconvolution method for each frequency and configuration. Several loops of imaging and self-calibration were undertaken for each data set to reduce the effects of phase and amplitude errors in the data. The final radio image at 4.8 GHz was obtained through combining the three VLA configurations and two observing frequencies. We have also produced a combined configuration image at 1.4 GHz but do not show it as the structure is remarkably similar to the 4.8 GHz image.

We have made a spectral index map between 1.4 GHz and 4.8 GHz to compare the spectral features more directly with the X-ray structure. This map was created from the combined configuration data at each frequency. The *uv*-coverage of both data sets was matched and both

frequencies were imaged with a $4.3''$ circular beam. We have blanked all pixels in the spectral index map that were lower than the 5σ level on either of the input maps.

4. IMAGES

Merged X-ray images of the source were created. The images were corrected using merged background images and exposure maps. An image showing the combined data from all CCD chips used in the analysis (ACIS S1, S2, S3, I2, and I3) in the 0.3 – 10.0 keV band is shown in Fig. 1. This figure illustrates the different roll angles that were used when the observations were performed. The extended cluster emission is visible, as well as numerous point sources which appear more extended while increasingly off-axis due to the larger PSF in these regions. The image has been smoothed with a $3''$ Gaussian.

An unsmoothed image in the 0.3 – 2.0 keV band of the central region of the cluster is shown in Fig. 2. The image reveals exquisite detail related to the interaction of the AGN with the ICM. Point sources, including the central AGN, are visible. Cavities or bubbles to the N and S of the AGN are seen, as well as outer cavities to the NW and SE. The inner cavities are bounded by bright, dense, rims, and the NW cavity is surrounded by a very narrow, filamentary loop. A filament extends into the N bubble. A shock is seen exterior to the bubbles and rims, and a probable second shock is visible to the NE.

A three-color image of the central $6'.56 \times 6'.56$ region of A2052 is displayed in Fig. 3. The image has been slightly smoothed, using a $1''.5$ Gaussian, and the scaling for each of the three colors is logarithmic. Red represents the soft (0.3 – 1.0 keV) band, green is medium (1.0 – 3.0 keV), and blue represents the hard band (3.0 – 10.0 keV). The bright rims surrounding the inner bubbles appear cool. The first shock exterior to the bubble rims is slightly elliptical with the major axis in the north-south direction (Blanton et al. 2009). It is visible as a discontinuity in the surface brightness, and the bluish color is consistent with a temperature rise in this region. Outside of the inner shock, a second surface brightness discontinuity is seen as greenish emission in this figure. The discontinuity is sharper to the NE and more extended to the SW. This feature may represent a shock or a cold front. These features will be explored in further detail in §6.

A composite X-ray/optical/radio image is shown in Fig. 4. The 0.3 – 2.0 keV *Chandra* image is shown in red, radio emission at 4.8 GHz from the VLA is displayed as blue, and optical r-band emission from the Sloan Digital Sky Survey (SDSS; Abazajian et al. 2009) is shown as green. The AGN is visible in the X-ray, radio, and optical, and the radio lobes fill the cavities in the X-ray emission. This includes the inner cavities as well as an outer cavity bounded by a narrow loop to the NW and the outer cavity to the S/SE. In addition, the radio emission is breaking through the northern bubble rim to the north. The X-ray filament extending from the northern bubble rim towards the AGN was found to be associated with $H\alpha$ emission in Blanton et al. (2001). In Fig. 5, we show SDSS r-band contours superposed on a *Chandra* image in the 0.3 – 10.0 keV range that has been smoothed with a $1''.5$ radius Gaussian. The central cD galaxy is oriented in the NE-SW direction in the optical. The inner bubbles seen in the X-ray emission are within the cD galaxy.

4.1. Residual Images

In order to better reveal features in the X-ray image, we created residual images using two different techniques. In the first, we used the method of unsharp-masking, and in the second, we subtracted a 2D beta model from the X-ray image. We find that unsharp-masking is useful for highlighting the structure in the inner parts of the cluster, while the model subtraction is better at revealing larger-scale features.

4.1.1. Unsharp-masking

We created an unsharp-masked image in the 0.3 – 10.0 keV energy range. Sources were detected in the image using the wavelet detection tool “wavdetect” in CIAO (Freeman et al. 2002). Several wavelet scales were used, at 1, 2, 4, 8, and 16 pixels, where 1 pixel = $0''.492$. Sources detected using this method were visually examined and several were rejected as being clumpy X-ray gas emission rather than point sources. A source-free image was created by replacing the source pixel values with the average value found in an annulus surrounding each source. We retained the sources in our unsharp-masked image while making corrections with a source-free image. Smoothed images, both with and without sources, were created by smoothing with a $0''.98$ radius Gaussian. Another copy of the source-free image was smoothed with a $9''.8$ Gaussian. A summed image was made by combining the source-free images smoothed at the two different scales. A difference image was made by subtracting the $9''.8$ Gaussian-smoothed source-free image from the $0''.98$ Gaussian-smoothed image that contained sources. Finally, the unsharp-masked image was created by dividing the difference image by the summed image. In this way, we retain the sources in the image, smoothed at a scale of $0''.98$. This method is similar to that in Fabian et al. (2006), although sources are excluded throughout in their unsharp-masked images.

The unsharp-masked image is displayed in Figure 6 with VLA 4.8 GHz radio contours superposed. The bubbles in the X-ray emission are more easily seen in this image, as are the bright bubble rims, the shock exterior to the bubble rims, and the second shock or cold front feature to the NE. The radio emission fills the inner bubbles and the southern lobe turns to fill the outer southern bubble. The radio lobe to the north appears to be escaping through a gap in the northern bubble rim, and a narrow filament is seen in the radio in this region. The radio emission also extends beyond the bubble rims to the NW to fill a small bubble bounded by a narrow X-ray filament. To the east, an extension in the radio fills a small depression in the X-ray on the scale of approximately $10''$.

4.1.2. Beta-model subtraction

A 2D beta model was used to fit the surface brightness in both 0.3 – 2.0 keV and 0.3 – 10.0 keV images using a circular region with radius $5''.66$. The images were source-free, with the surface brightness at the position of sources approximated from the surface brightness in an annulus around each source, as above. Corrections were made for exposure, using a merged exposure map. Similar results were obtained for the fits to the images in both energy bands. Errors were computed using Cash statistics. For

the 0.3 – 2.0 keV image, the center of the large scale emission was found to be only $1''.2$ away from the position of the AGN. The emission was found to be slightly elliptical, with an ellipticity value of 0.18 ± 0.00081 (where ellipticity values range from 0 to 1, with 0 indicating circular emission). The position angle for the semi-major axis of the ellipse is $38.2 \pm 0.1^\circ$ measured north towards east. The core radius using this model is $25.1 \pm 0.060''$ and the beta index is $\beta = 0.46 \pm 0.00021$.

The residual image after 2D beta model subtraction in the 0.3 – 2.0 keV band is shown in Fig. 7. The image has been smoothed with a $7''.38$ radius Gaussian. The smoothing washes out the details in the very center of the image, but the bright bubble rims are clearly visible. A spiral feature is seen, starting in the SW and extending to the NE. Similar spiral structures have been seen in other clusters, with A2029 being a particularly clear example (Clarke et al. 2004).

5. X-RAY SPECTRAL MAPS

Spectral maps were created to examine the distribution of temperature, as well as entropy, pressure, and abundance using the technique described in Randall et al. (2008, 2009b). The temperature maps were created by extracting spectra for the separate *Chandra* observations and fitting them simultaneously in the 0.6 – 7.0 keV range with a single temperature APEC model, with N_H set to the Galactic value of $2.71 \times 10^{20} \text{ cm}^{-2}$ (Dickey & Lockman 1990) and the abundance allowed to vary. Background spectra were extracted from the blank sky background observations that were reprojected to match each data set. Data from both the frontside- and backside-illuminated (FI and BI) chips were used, with separate response files and normalizations determined for each ObsID’s data set, with the FI and BI normalizations allowed to vary independently for each ObsID. Spectra were extracted with a minimum of either 2000 or 10000 background-subtracted counts, corresponding to a minimum SNR of approximately 45 or 100, respectively, depending on our analysis goals. The radius of the circular extraction region was allowed to grow to the size required to extract the minimum counts. Spectral maps of the central region of A2052 were previously presented in Blanton et al. (2003, 2009). Here, with the much deeper *Chandra* data, we are able to examine a much larger region of the cluster with high precision. We have chosen to include spectral maps created as described above rather than Voronoi-Tessellation maps, even though some of the map pixels are not independent (some regions used in spectral fitting overlap), especially in the outer regions of the maps. We find that spectral structures are easier to see on the maps we present, and they are confirmed by extracting spectral profiles in §6 and §7.

In Fig. 8, we display a high-resolution ($0''.492$ pixels) temperature map of the central region of A2052, where the minimum number of net counts was 2000. Superposed on the temperature map are X-ray surface brightness contours derived from the $1''.5$ Gaussian-smoothed 0.3 – 10.0 keV image. The coolest parts of the cluster are found in the brightest parts of the X-ray rims surrounding the bubbles, including the bright rim to the W and NW, the E-W bar that passes through the cluster center and AGN, and the N filament that extends into the N bubble. An overlay of $H\alpha$ contours from McDonald et

al. (2010) onto the high-resolution temperature map is shown in Fig. 9. For comparison, the $H\alpha$ contours are superposed onto the 0.3 – 10.0 keV, $1''.5$ radius Gaussian smoothed, *Chandra* image in Fig. 10. The correspondence between the $H\alpha$ emission and both the surface brightness and temperature structure is excellent. $H\alpha$ emission, representing gas with $T \approx 10^4$ K, is detected in the brightest and coolest structures in the cluster center, including the E-W bar and the filament that extends into the N bubble. While correspondence between $H\alpha$ and X-ray surface brightness was shown in Blanton et al. (2001), with the deeper *Chandra* and new $H\alpha$ data presented here, we see more detail in the association, including the filament extending into the N bubble not reaching the AGN (whereas it appeared to reach the AGN in $H\alpha$ in the Baum et al. (1988) data shown in Blanton et al. (2001)). The association between the $H\alpha$ and X-ray indicates that at least some gas is cooling from the temperature associated with the X-ray gas in these regions ($T \approx 10^7$ K) to $T \approx 10^4$ K. McDonald et al. (2010) and McDonald et al. (2011) suggested that this gas represents gas that was previously cooler and then ionized to produce the $H\alpha$ emission. Given the low UV-to- $H\alpha$ ratio in this system, they conclude that the ionization source would likely be shocks related to the AGN rather than nearby, luminous, stars, as in some other cluster centers.

Additionally, significant clumpy substructure in the temperature distribution is seen in the gas throughout the central cluster region. This substructure will be further investigated in an upcoming paper. Errors range from approximately 2% in the very central, brightest regions, to approximately 12% in the outer areas of the map.

In Fig. 11, we show a projected or “pseudo” pressure map of the central region of A2052. The map was derived using the APEC normalization and temperature from the spectral fits that resulted in the temperature map in Fig. 8. The APEC normalization is proportional to n^2V , where n is density and V is the volume projected along the line of sight. We define the projected pressure as $kT(A)^{1/2}$, where A is the APEC normalization scaled by area to account for extraction regions that may go off the edge of the chips. Superposed on the pressure map are X-ray surface brightness contours in the 0.3 – 10.0 keV band. The most obvious feature in the map is the clear ring of high pressure that is coincident with the inner discontinuity seen in surface brightness and the jump in density (Blanton et al. 2009) visible in Figs. 2 and 3. The bubbles, including the inner bubbles to the N and S of the AGN as well as the outer, small NW bubble and the outer SE bubble, are visible as lower-pressure regions in this projected pressure map since they are largely devoid of X-ray-emitting gas.

A lower-resolution temperature map covering a larger region of the center is shown in Fig. 12. Here, the minimum number of background-subtracted counts is 10000, and the pixel size is $8''$. The errors in temperature range from 1% in the inner regions to 5% in the outskirts of the frame. Superposed are the residual surface brightness contours in the 0.3 – 2.0 keV band after beta-model subtraction (see Fig. 7). The spiral excess traces out a region of temperature lower than its surroundings. In addition, this low temperature feature continues inward

along the direction of the spiral toward the cluster center, beyond the extent of the inner spiral contours.

A higher-resolution temperature map showing the same f.o.v. as in Fig. 12 is displayed in Fig. 13. The spectra were extracted with a minimum of 2000 background-subtracted counts, and the pixel size is $4''$. The map represents more than 80000 spectral fits. Here, the errors range from 2% in the inner regions to approximately 14% in the outskirts. Two views of a pseudo-pressure map derived from the fits that were used to make the temperature map in Fig. 13 are shown in Figs. 14 and 15. The pressure jump corresponding to the innermost shock is clearly seen, as well as evidence for pressure structure tracing the second inner shock (seen in the outer X-ray contour). There is no evidence of structure in the pressure map related to the spiral structure.

A pseudo-entropy map is displayed in Fig. 16 with excess surface brightness contours after subtracting a beta model superposed. The map was derived using the spectral fits that resulted in the temperature map in Fig. 13. We define pseudo-entropy as $kT(A)^{-1/3}$, with A defined as above. In general, the entropy decreases toward the cluster center. There appears to be correspondence between structure in the entropy map and the spiral feature.

A projected abundance map is shown in Fig. 17, corresponding to the temperature map in Fig. 12 with $8''$ pixels and a minimum of 10000 background-subtracted counts per pixel. Errors range from 5% in the highest surface brightness regions, to 23% in the outer regions of the map (with the majority of the errors at the 10 – 15% level across the map). To the SW, a region of high abundance is coincident with the high surface-brightness spiral. This is consistent with higher metallicity gas sloshing away from the cluster center, creating the spiral. A high-metallicity region was found at a similar position to the SW using *XMM-Newton* data (de Plaa et al. 2010).

6. INNER SHOCK FEATURES

In Blanton et al. (2009), we identified two inner surface brightness jumps that were likely associated with shocks. These jumps are visible in Figs. 3, 6, and 15. The first inner jump extends around the cluster center in a slightly elliptical shape in the N-S direction at a radius of approximately $40''$. The second jump is elliptical in the NE to SW direction, and is sharper and at a smaller radius from the AGN in the NE direction. To the NE, the second jump is at a radius of approximately $65''$.

Similar to Blanton et al. (2009), we have fitted a projected spherical density model to the surface brightness in a NE wedge with PA -2° to 98° measured east from north. The projected model characterizes the density using power laws and discontinuous jumps. We use three power laws, and identify two density jumps. See Randall et al. (2008) for further description of this technique.

Our results are generally consistent with, and a refinement of, those presented in Blanton et al. (2009). The density jumps are at radii of 44.2 ± 0.1 arcsec (31.2 ± 0.1 kpc) and $66.3^{+0.3}_{-0.06}$ arcsec ($46.8^{+0.02}_{-0.04}$ kpc), respectively, from the AGN. The magnitudes of the jumps are factors of $1.25^{+0.016}_{-0.015}$ and $1.29^{+0.010}_{-0.012}$, for the first and second jumps, respectively. The slopes of the three power-law components, going from the inner to outer regions, are

$-0.53^{+0.029}_{-0.024}$, $-1.25^{+0.030}_{-0.037}$, and $-1.06^{+0.0067}_{-0.0084}$.

The jumps in density correspond to Mach numbers of $1.17^{+0.011}_{-0.010}$ and $1.20^{+0.0072}_{-0.0079}$, respectively, for the first and second jumps. The temperature is then expected to rise a similar amount inside both shocks (a factor of 1.16 for the first shock and 1.19 for the second shock).

We have calculated a deprojected temperature profile for the NE region, shown in Fig. 18. Dashed lines indicate the locations of the two shocks. As with all of our spectral fits, spectra were extracted separately for each data set and fitted simultaneously in XSPEC v12.6. The fits were performed in the 0.6 – 7.0 keV range. A single APEC model plus Galactic absorption was fitted to the outermost annulus spectra with abundance allowed to vary. The contribution of emission from this shell to the next annulus in was calculated using geometric projection, assuming spherically symmetric shells, and the APEC normalization scaled appropriately to account for the projection of this outer component. The parameters for the contribution from the outer annulus were frozen, and an additional APEC model was added for the annulus of interest. This procedure was continued inward, where the spectral model for each annulus included contributions from all external annuli. See Blanton et al. (2003) for further description.

In addition, in Fig. 18, we present density and pressure profiles for the NE region. The density and pressure were determined from the deprojected spectral fits, since the normalization of the free APEC component for each annulus is proportional to the square of density at that annulus. Note that the radius range extends to approximately 300'' (212 kpc) where the overdensity (the density relative to the critical density) is ≈ 12500 . For comparison, an overdensity of 500 (r_{500}) is at $r \approx 800$ kpc ($\approx 1100''$).

A clear rise in temperature is seen inside the innermost shock, in addition to the jumps in density and pressure in this region. In Blanton et al. (2009), while the temperatures inside and outside this shock were consistent with the rise expected given the Mach number, the best-fitting temperatures were approximately flat across the shock. Here, with the much deeper data set, the rise is clearly detected. Just outside the shock, the temperature is $kT = 2.81^{+0.11}_{-0.15}$ keV, while inside the shock it reaches $kT = 3.14^{+0.11}_{-0.11}$ keV, a factor of $1.12^{+0.10}_{-0.08}$ higher, with a significance of 2.1σ . Such temperature rises associated with weak shocks are extremely difficult to measure in cluster centers, with very deep, high resolution observations required.

For the second shock, the situation is less obvious. The best-fitting temperatures are approximately flat across the shock: $kT = 3.35^{+0.20}_{-0.16}$ keV outside the shock and $kT = 3.27^{+0.14}_{-0.15}$ keV inside the shock. Therefore, even within the errors, this is inconsistent with the expected temperature jump of 1.19, with the highest rise permitted giving a factor of 1.07. However, as noted above, temperature rises associated with weak shocks are very difficult to detect, and due to projection effects, measured rises are expected to be lower than might be expected based on shock strengths alone (e.g. Randall et al. 2011). In addition, the gas may cool due to adiabatic expansion (McNamara & Nulsen 2007). Also, we note that the temperature drops precipitously in the next annulus

inward from the annulus just inside the shock boundary. This may indicate that the temperature of the gas just inside the shock boundary was also previously much lower before being shocked, and then the rise in temperature in this region may be higher than we have estimated above.

In addition, we fitted a projected density model to the surface brightness profile in a wedge to the SW with PA 250° to 340° from N out to a radius of 100'' to characterize the inner shocks in this direction. We find similar results to the SW as we did to the NE for the first inner shock. We find a density jump of a factor of 1.26 ± 0.025 at a radius of 48 ± 0.4 arcsec (34 ± 0.3 kpc). However, as can be seen in the surface brightness distribution in the images (i.e. Fig. 3), the second inner shock edge seems less sharp and extends to larger radii in the SW than in the NE. We do not find a density jump corresponding to the second inner shock to the SW, only a change in slope at a radius of 107 arcsec (75.5 kpc).

7. SPIRAL FEATURE

The spiral feature visible in Fig. 7 is similar to that seen in simulations of gas sloshing in cluster centers (Ascasibar & Markevitch 2006). The sloshing sets up cold fronts and the distinctive spiral morphology. We therefore would expect the excesses seen in Fig. 7 to be visible as excesses in surface brightness profiles containing these regions. Temperature profiles should show cooler gas coincident with the surface brightness enhancements. In addition, the simulations predict that the bright, sloshing, spiral region will contain gas of lower entropy as cluster central gas is displaced to larger radii. As shown in §5, the spiral excess is coincident with regions of low temperature and entropy in projected maps.

We have extracted surface brightness profiles from wedges in three directions: SW, NE, and NW. The SW corresponds to the bright, inner part of the spiral, while the NE includes the outer region of the spiral, and the NW is largely free from any spiral excess emission and serves as a comparison region. The sectors used for the profiles are shown superposed on the 0.3 – 2.0 keV residual image in Fig. 19. The surface brightness profiles for the three regions are shown in Fig. 20. Error bars are smaller than the symbols. Relative to the NW, non-spiral region, the SW shows excess emission from approximately 60'' – 195'' (42 – 138 kpc), corresponding to the inner part of the spiral. To the NE, excess emission is seen beyond approximately 110'' (78 kpc). Note that the enhancement in the NW in the ≈ 10 – 20'' (7 – 14 kpc) region shows that the bubble rims are brightest in this region, which also corresponds to cooler gas seen in $H\alpha$ (Figs. 9, 10).

We have extracted spectra in the three wedges and determined projected temperature profiles. The spectra were extracted separately for each of the observations as well as for the corresponding background files. The spectra for each region were fitted simultaneously using an APEC thermal plasma model. Absorption was fixed at the Galactic value and elemental abundances were allowed to vary. Projected temperature profiles comparing the SW and NW (non-spiral) regions and the NE and NW regions are shown in Figs. 21 and 22, respectively. In both cases, significant drops in temperature are seen in the regions corresponding to the surface-brightness ex-

cesses associated with the spiral described above. In addition, the high surface brightness $\approx 10'' - 20''$ (7 – 14 kpc) region in the NW has cooler temperatures than those radii regions to the SW and NE. This is likely due, at least in part, to the larger contribution to the emission measure from the bright, compressed, cool, bubble rims to the NW at these radii as compared to the same radii to the SW and NE, where the bubble rims are not as bright.

In order to examine the bright region of the spiral to the SW in more detail, we have fitted a projected density model to the surface brightness profile, as described above for the NE sector shock fits. To focus on the cold front / spiral edge, we fit only regions with $r > 70''$. We find a density jump of a factor of $1.12^{+0.022}_{-0.011}$ at a radius of 154 ± 1.5 arcsec (109 ± 1 kpc) from the cluster center.

We extracted spectra in larger bins to the SW, and performed a spectral deprojection as described above for the NE. Profiles of temperature, density, and pressure are shown in Fig. 23. Dashed lines, going from smaller to larger annuli, indicate the positions of the first inner shock, the second inner shock / edge, and the exterior edge of the cold front / SW spiral. Since the deprojection introduces some scatter, particularly in the region between the inner shocks, we have also plotted the projected temperature profile as well as the pressure profile using the projected temperatures (shown as open circles). A temperature rise is seen associated with the first inner shock, but not the second inner shock. A clear density fall off is seen at the outer edge of the SW spiral. The temperatures within the spiral region are cooler than those outside of it.

Projected abundance profiles to the SW and NE are shown in Fig. 24. The dashed line marks the outer edge of the spiral to the SW (at $r = 154''$, as determined above). The abundance is higher in the bright, SW, spiral region, than in the corresponding radial region to the NE. Profiles of entropy for the SW and NE regions are shown in Fig. 25. The entropy is defined as $S = kT/n_e^{2/3}$, and projected temperature values were used. As in Fig. 24, the outer edge of the SW spiral region is marked with a dashed line. There is clearly a cross-over in the entropy profiles for the SW and NE regions near this radius. From $r \approx 70 - 150''$, low entropy values are found coincident with the SW spiral excess. In the NE, the spiral excess is at larger radii, and this is seen in the entropy profile, where the values are low in the NE with radii greater than approximately $190''$. This is striking confirmation of the predictions from sloshing models, where central, low entropy, cluster gas is displaced to larger radii (i.e. Ascasibar & Markevitch 2006).

The sum of the evidence, including the surface brightness profiles, and temperature, abundance, and entropy distributions, points to the spiral being a cold front / sloshing feature resulting from an off-axis merger earlier in the cluster's history.

8. X-RAY CAVITIES

Clear cavities (or “bubbles”) in the X-ray emission are seen in the *Chandra* images to the N and S of the AGN. In addition, there is a small bubble bounded by a narrow X-ray filament to the NW and a bubble separated from the S bubble to the SE. A very small depression is also

seen to the E. These features are all filled with 4.8 GHz radio emission as seen in Fig. 6. As described in §3, we created a radio spectral index map using the 1.4 and 4.8 GHz VLA data. The map is shown in Fig. 26 with contours of $1''5$ Gaussian-smoothed X-ray emission in the 0.3 – 10.0 keV band superposed.

The spectral index is flattest at the position of the radio and X-ray core, and steepens into the radio lobes. The regions we have identified as outer bubbles, to the NW and SE, are associated with regions with distinctly steeper spectral indices. This is consistent with these bubbles resulting from an earlier stage in the current outburst, or from a separate, earlier AGN outburst, since the high-energy electrons age faster than the lower energy electrons, resulting in steepening of the spectrum over time. The radio emission “leaking” out of the N bubble through the bubble rim directly N of the AGN has a spectral index consistent with that filling the N lobe, making it likely that this emission is part of the current AGN outburst.

Obvious additional bubbles are not seen outside of this central region in the images, including the unsharp-masked images. Also, lower frequency radio emission at 330 MHz (Zhao et al. 1993) has a similar extent as the 1.4 and 4.8 GHz emission. To search for more bubbles at larger radii, we have made a pressure-difference map. The map was created by fitting a 2D beta model to a pressure map with $8''$ bins, and a minimum of 10000 background-subtracted counts for each region used for a spectral fit. This corresponds to the temperature map shown in Fig. 12. The center was fixed to the position found in the 2D beta model fit to the surface brightness, described in 4.1.2. The values for the ellipticity and position angle of the ellipse, 0.17 and 119° from W, respectively, were similar to those found for the surface brightness fit. The pressure-difference map is shown in Fig. 27, with 4.8 GHz radio contours superposed. Regions of low pressure are evident to the N and S of the AGN, along the current axis of the radio source. For both the N and S apparently low-pressure regions on the map, we have extracted spectra within circular apertures covering the regions, as well as comparison regions in surrounding circular annuli. We have calculated “projected” pressures, defined as $kT(A)^{1/2}$, where A is the APEC normalization, for the apparent bubbles (low pressure regions) and the comparison annuli. For the N bubble, we find a significance in the lower projected pressure of 2.3σ compared to the comparison annulus, and for the S bubble, the significance is 2.2σ . These regions of lower pressure may represent outer bubbles from an earlier outburst (or multiple earlier outbursts) of the AGN. Future higher dynamic range radio data may give further evidence that these features are related to AGN activity.

Approximating both of these possible bubbles as spheres with radii of 34 kpc, located 75 kpc from the cluster center, we calculate their energy input into the ICM as $E = 4PV$ (Churazov et al. 2002). This assumes that the bubbles are filled with relativistic plasma ($\gamma = 4/3$). Using the average pressure at the cluster radius of 75 kpc of $P \approx 6 \times 10^{-11}$ dyn cm $^{-2}$, we find that each bubble can add 1×10^{60} erg to the ICM.

9. DISCUSSION AND CONCLUSIONS

We have presented first results from a very deep *Chandra* observation of Abell 2052. Detailed structure is seen in the inner part of the cluster, including bubbles, bright shells, and filaments. Radio emission at 4.8 GHz is seen to fill bubbles to the N and S of the AGN, as well as outer bubbles to the NW and SE, and a small bubble to the E. $H\alpha$ emission is coincident with the brightest and coolest regions in the cluster center, including the E-W bar and the filament in the N bubble, indicating that at least some gas is cooling to $T \approx 10^4$ K.

An inner shock is clearly seen surrounding the cluster center, as well as a second feature exterior to the first that is also most likely a shock. Both edges in surface brightness can be described as arising from shocks with Mach numbers ≈ 1.2 . For the inner shock, evidence for an associated temperature rise is seen in a three-color image. Also, a temperature profile reveals a significant increase inside this region, consistent with that expected given the shock strength. Such temperature rises associated with weak shocks driven by AGN in the centers of cool core clusters have only rarely been measured, given the narrow widths of the shocks, the small magnitudes of the temperature rises, and the cooling related to adiabatic expansion and the projection of cluster gas at larger radii.

A spiral feature is seen, and is well-described as resulting from gas sloshing related to a cluster-cluster or sub-cluster merger earlier in the lifetime of A2052. There is also evidence of dynamical activity in the cluster from optical spectroscopy: the central cD has a fairly large peculiar velocity (290 ± 90 km s $^{-1}$) relative to the cluster mean (Oegerle & Hill 2001). The X-ray spiral is brightest to the SW, and continues around the cluster center to the E and NE. The SW portion of the excess emission was shown in Laganá et al. (2010) using a shorter *Chandra* exposure, and in de Plaa et al. (2010) using a deep *XMM-Newton* observation. The spiral structure was not seen, however, before this very deep *Chandra* observation. Laganá et al. presented several residual *Chandra* images of cool core clusters, and noted that A2052 was an exception in not exhibiting a spiral feature in the available data, and de Plaa et al. described the SW excess as a cold front. Here, in addition to exhibiting an excess in surface brightness on a 2D model-subtracted *Chandra* image, the brightness distribution is confirmed using surface brightness profiles in different sectors across the image. The spiral is also shown to contain gas cooler

than its surroundings in both temperature maps and sector profiles. Regions of low entropy are found coincident with the spiral surface-brightness excess. Finally, the abundance is higher in the spiral region than its surroundings. This is consistent with central, low-entropy, high-metallicity gas sloshing out to larger radii. Therefore, sloshing can play a part in redistributing the metals within a cluster (Simionescu et al. 2010, de Plaa et al. 2010). Outbursts from the AGN also play a role in metal redistribution (Kirkpatrick et al. 2009). Detailed measurements of the spectral properties of similar diffuse spiral excesses have only rarely been measured. While Laganá et al. (2010), for example, presented evidence of excess surface-brightness spirals in several systems, in many cases temperature declines were not detected associated with the spiral features, and if they were, they were most often only measured for the bright, inner spiral regions.

While the radio emission shows clear correspondence with deficits in the X-ray emission, and the extended radio structure is likely related to typical radio lobes from the AGN, there may be some component of radio mini-halo emission. A correlation has been found between the presence of sloshing features in clusters and mini-halos (ZuHone, Markevitch, & Brunetti 2011), and these mini-halos may result from reacceleration of relativistic electrons by turbulence associated with sloshing (Mazzotta & Giacintucci 2008). With our current radio data, however, we do not see obvious correspondence between the radio emission and the spiral sloshing feature.

There is evidence for outer bubbles related to one or more earlier outbursts from the AGN. While not seen in the surface brightness images, deficits are evident in a pressure-residual map after subtracting off a model of the average pressure distribution. The deficits are seen to the N and S of the cluster center, in line with the current axis of the radio lobes. Each of these bubbles could inject up to 1×10^{60} erg into the intracluster medium.

Support for this work was provided by the National Aeronautics and Space Administration, through *Chandra* Award Number GO9-0147X. Basic research in radio astronomy at the Naval Research Laboratory is supported by 6.1 Base funding. SWR was supported in part by the Chandra X-ray Center through NASA contract NAS8-03060. We thank Frazer Owen for useful discussions.

REFERENCES

- Ascasibar, Y. & Markevitch, M. 2006, *ApJ*, 650, 102
 Abazajian, K. N. et al. 2009, *ApJS*, 182, 543
 Baum, S. A., Heckman, T. M., Bridle, A., van Breugel, W. J. M., & Miley, G. K. 1988, *ApJS*, 68, 643
 Blanton, E. L., Sarazin, C. L., McNamara, B. R., & Wise, M. W. 2001, *ApJ*, 558, L15
 Blanton, E. L., Sarazin, C. L., & McNamara, B. R. 2003, *ApJ*, 585, 227
 Blanton, E. L., Randall, S. W., Douglass, E. M., Sarazin, C. L., Clarke, T. E., & McNamara, B. R. 2009, *ApJ*, 697, L95
 Blanton, E. L., Clarke, T. E., Sarazin, C. L., Randall, S. W., & McNamara, B. R. 2010, *PNAS*, 107, 7174
 Baum, S. A., Heckman, T. M., Bridle, A., van Breugel, W. J. M., & Miley, G. K. 1998, *ApJS*, 68, 643
 Böhringer, H., et al. 1993, *MNRAS*, 264, L25
 Churazov, E., Sunyaev, R., Forman, W., & Böhringer, H. 2002, *MNRAS*, 332, 729
 Clarke, T. E., Blanton, E. L., & Sarazin, C. L. 2004, *ApJ*, 616, 178
 de Plaa, J., et al. 2010, *A&A*, in press
 Dickey, J. M. & Lockman, F. J. 1990, *ARA&A*, 28 215
 Fabian, A. C., et al. 2003, *MNRAS*, 344, L43
 Fabian, A. C., et al. 2006, *MNRAS*, 366, 417
 Forman, W., et al. 2005, *ApJ*, 635, 894
 Forman, W., et al. 2007, *ApJ*, 665, 1057
 Freeman, P. E. et al. 2002, *ApJS*, 138, 185
 Huang, Z. & Sarazin, C. L. 1998, *ApJ*, 496, 728
 Laganá, T. F., Andrade-Santos, F., & Lima Neto, G. B. 2010, *A&A*, 511, A15
 Kirkpatrick, C. C. et al. 2009, *ApJ*, 707, L69
 Mazzotta, P. & Giacintucci, S. 2008, *ApJ*, 675, L9
 McDonald, M., Veilleux, S., Rupke, D. S. N., & Mushotzky, R. 2010, *ApJ*, 721, 1262
 McDonald, M., Veilleux, S., Rupke, D. S. N., Mushotzky, R., & Reynolds, C. 2011, *ApJ*, in press
 McNamara, B. R., et al. 2000, *ApJ*, 534, L135
 McNamara, B. R., et al. 2005, *Nature*, 7021, 45

- McNamara, B. R. & Nulsen, P. E. J. 2007, *ARA&A*, 45, 117
- Million, E. T., et al. 2010, *MNRAS*, 407, 2046
- Mittal, R., Hudson, D. S., Reiprich, T. H., & Clarke, T. 2009, *A&A*, 501, 835
- Nulsen, P. E. J., McNamara, B. R., Wise, M. W., & David, L. P. 2005a, *ApJ*, 628, 629
- Nulsen, P. E. J., et al. 2005b, *ApJ*, 625, L9
- Oegerle, W. R. & Hill, J. H. 2001, *AJ*, 122, 2858
- Peres, C. B. et al. 1998, *MNRAS*, 298, 416
- Peterson, J. R. et al. 2003, *ApJ*, 590, 207
- Randall et al. 2008, *ApJ*, 688, 208
- Randall et al. 2009a, *ApJ*, 700, 1404
- Randall et al. 2009b, *ApJ*, 696, 1431
- Randall et al. 2011, *ApJ*, 726, 86
- Rizza, E., et al. 2000, *AJ*, 119, 21
- Simionescu, A. et al. 2010, *MNRAS*, 405, 91
- Tamura, T. et al. 2008, *PASJ*, 60, 695
- Werner, N. et al. 2010, *MNRAS*, 407, 2063
- White, D. A., Jones, C., & Forman, W. 1997, *MNRAS*, 292, 419
- White, D. A. 2000, *MNRAS*, 312, 663
- Wise, M. W., McNamara, B. R., Nulsen, P. E. J., Houck, J. C., David, L. P. 2007, *ApJ*, 659, 1153
- Zhao, J.-H., Sumi, D. M., Burns, J. O., & Duric, N. 1993, *ApJ*, 416, 51
- ZuHone, J. A., Markevitch, M., & Johnson, R. E. 2010, *ApJ*, 717, 908
- ZuHone, J., Markevitch, M., & Brunetti 2011, *arXiv:1101.4627*

TABLE 1
Chandra X-ray Observations

Obs ID	Date	Roll Angle (deg)	Data Mode	Exp (ksec)
890	2000-09-03	265.1	FAINT	37.23
5807	2006-03-24	98.9	VFAINT	128.63
10477	2009-06-05	221.2	VFAINT	62.03
10478	2009-05-25	208.2	VFAINT	120.67
10479	2009-06-09	217.1	VFAINT	65.76
10480	2009-04-09	112.2	VFAINT	20.15
10879	2009-04-05	112.2	VFAINT	82.21
10914	2009-05-29	208.2	VFAINT	39.36
10915	2009-06-03	221.2	VFAINT	15.16
10916	2009-06-11	217.1	VFAINT	35.47
10917	2009-06-08	217.1	VFAINT	55.99

TABLE 2
VLA RADIO OBSERVATIONS

Obs. Code	Date	VLA Configuration	Frequency (MHz)	Bandwidth (MHz)	Duration (hours)
AS355	1988-11-30	A	4835.1/4885.1	50/50	3.0
AS355	1989-03-30	B	4835.1/4885.1	50/50	2.4
AS355	1989-06-26	C	4835.1/4885.1	50/50	2.6
AS355	1988-11-30	A	1464.9/1514.9	50/50	3.0
AS355	1989-03-30	A	1464.9/1514.9	50/50	2.1

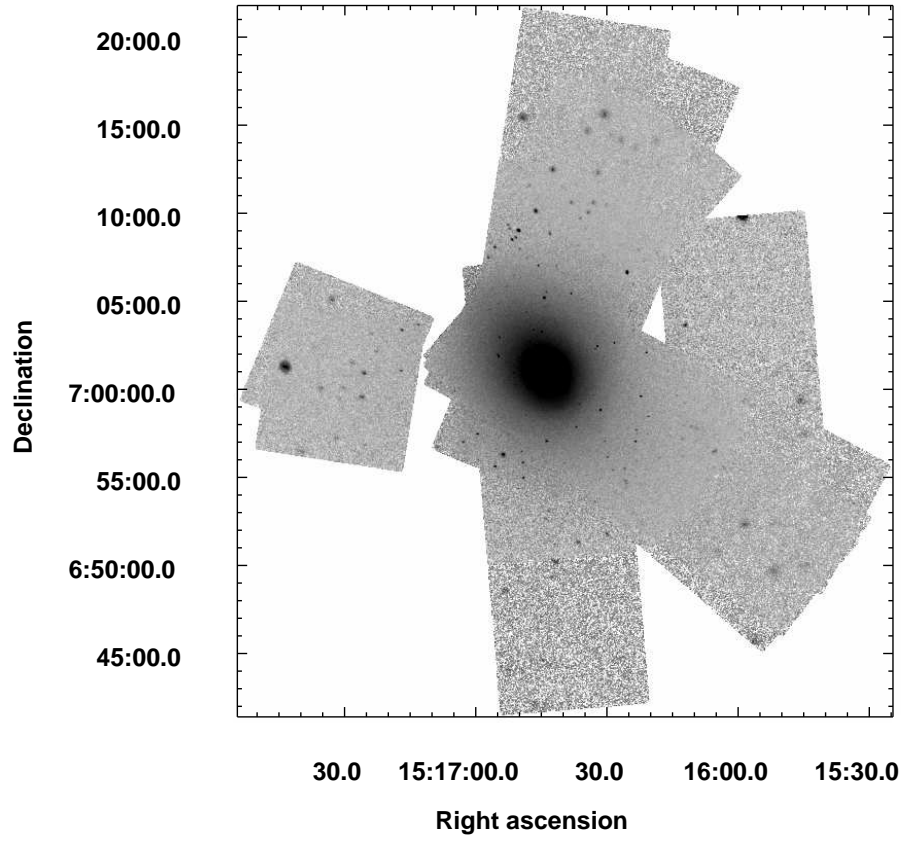


FIG. 1.— *Chandra* ACIS image of A2052 in the 0.3–10.0 keV band showing all CCD chips used in the analysis (the S4 chip was excluded) and illustrating the different roll angles used in the observations.

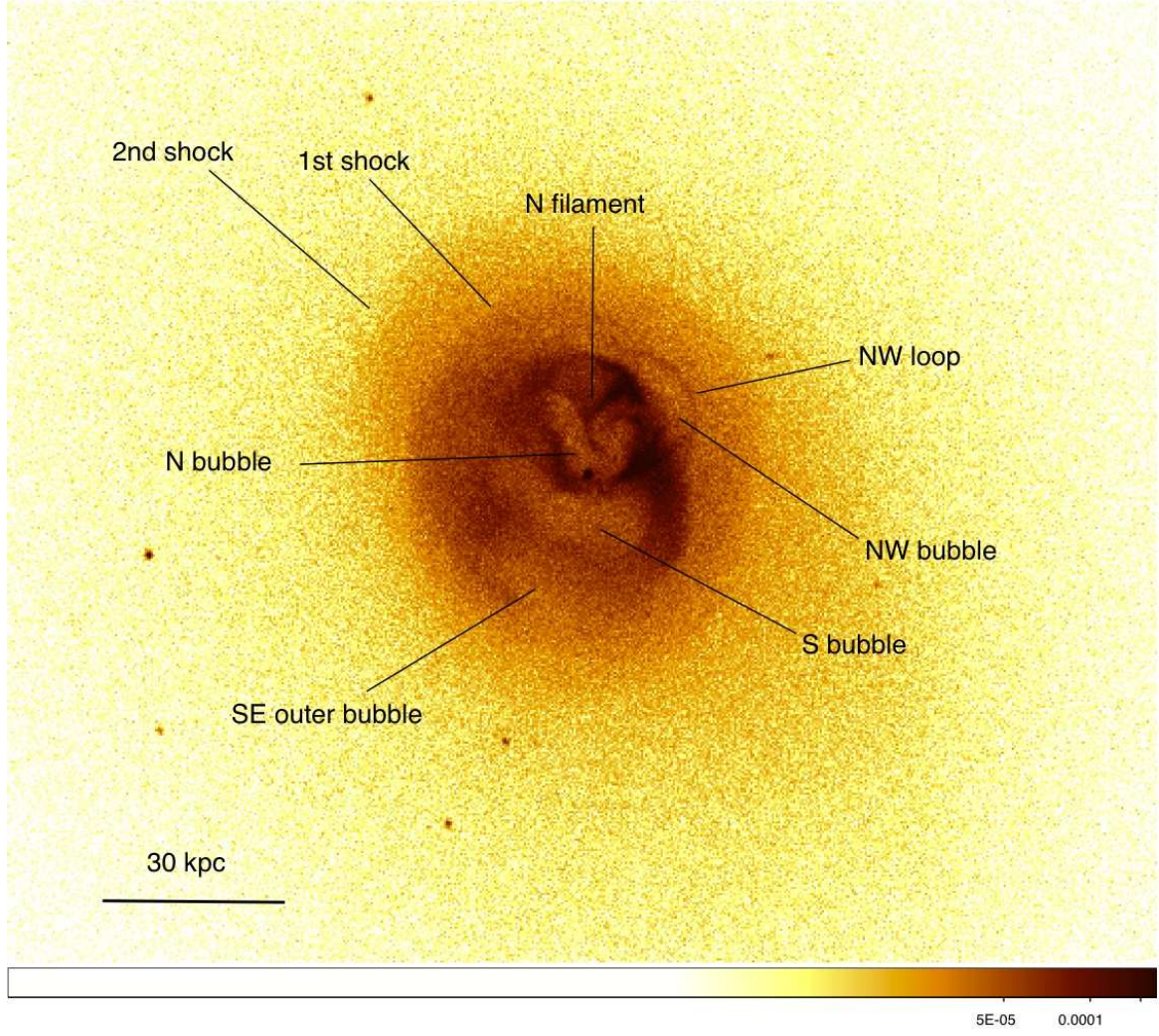


FIG. 2.— Unsmoothed *Chandra* image in the 0.3 – 2.0 keV band of the central region of A2052. The image reveals detailed structure related to the interaction of the AGN with the ICM, with important features labeled.

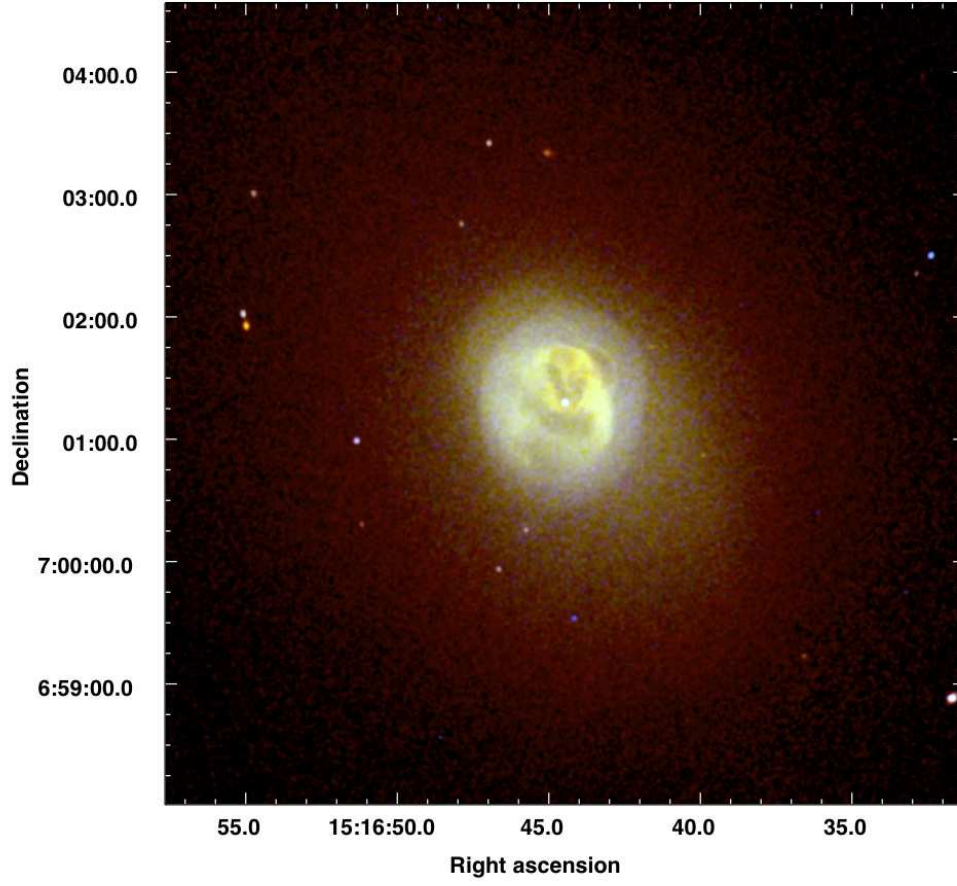


FIG. 3.— Three-color *Chandra* image of A2052. Red is 0.3 – 1.0 keV, green is 1.0 – 3.0 keV, and blue is 3.0 – 10.0 keV. Cavities are visible to the north and south of the AGN, surrounded by bright rims. Exterior to the bright rims, a slightly N-S elliptical shock is seen with hard (blue) emission.



FIG. 4.— Composite *Chandra* X-ray (red), VLA 4.8 GHz (blue), and SDSS r-band (green) $6'.6 \times 5'.8$ image of Abell 2052.

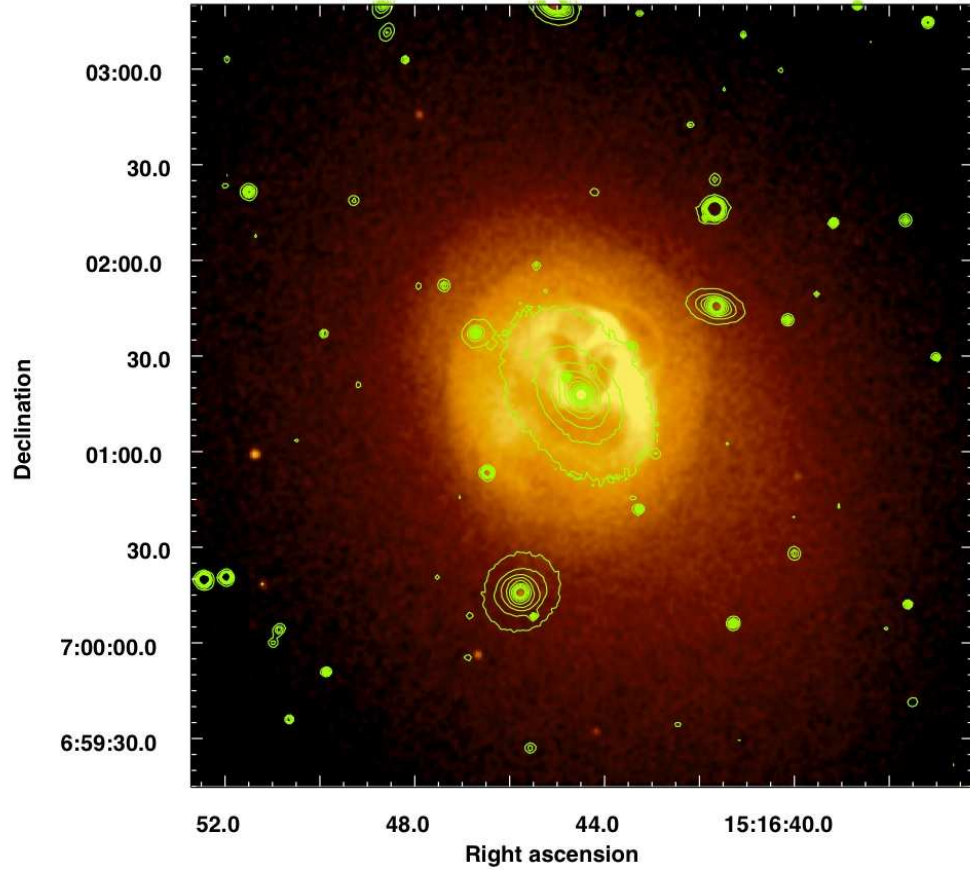


FIG. 5.— *Chandra* image in the 0.3 – 10.0 keV band, smoothed with a $1''.5$ radius Gaussian, with contours of optical r-band emission from the SDSS superposed.

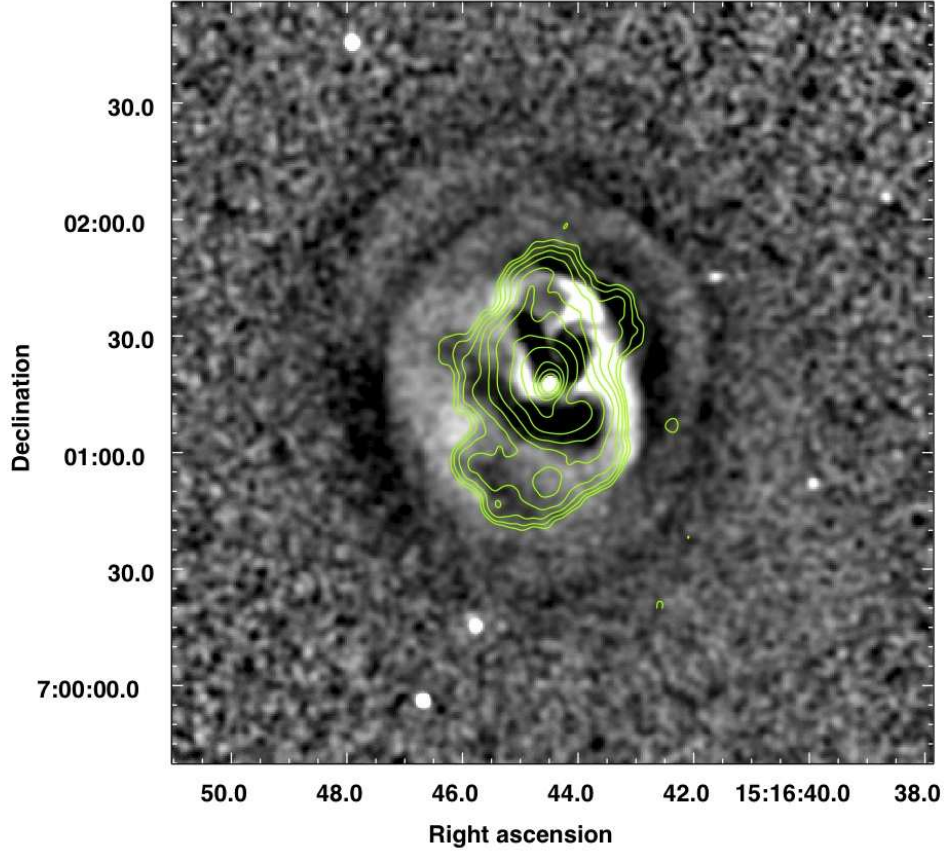


FIG. 6.— Unsharp-masked *Chandra* 0.3 – 10.0 keV image of A2052 with 4.8 GHz radio contours superposed. Radio emission fills X-ray cavities to the N and S, as well as outer cavities to the NW, S-SE, and E. The cavities are surrounded by X-ray bright rims. A filament extends into the N cavity, and a narrow filament surrounds the NW hole. Ripple-like features are seen surrounding the cluster center, corresponding to weak shocks.

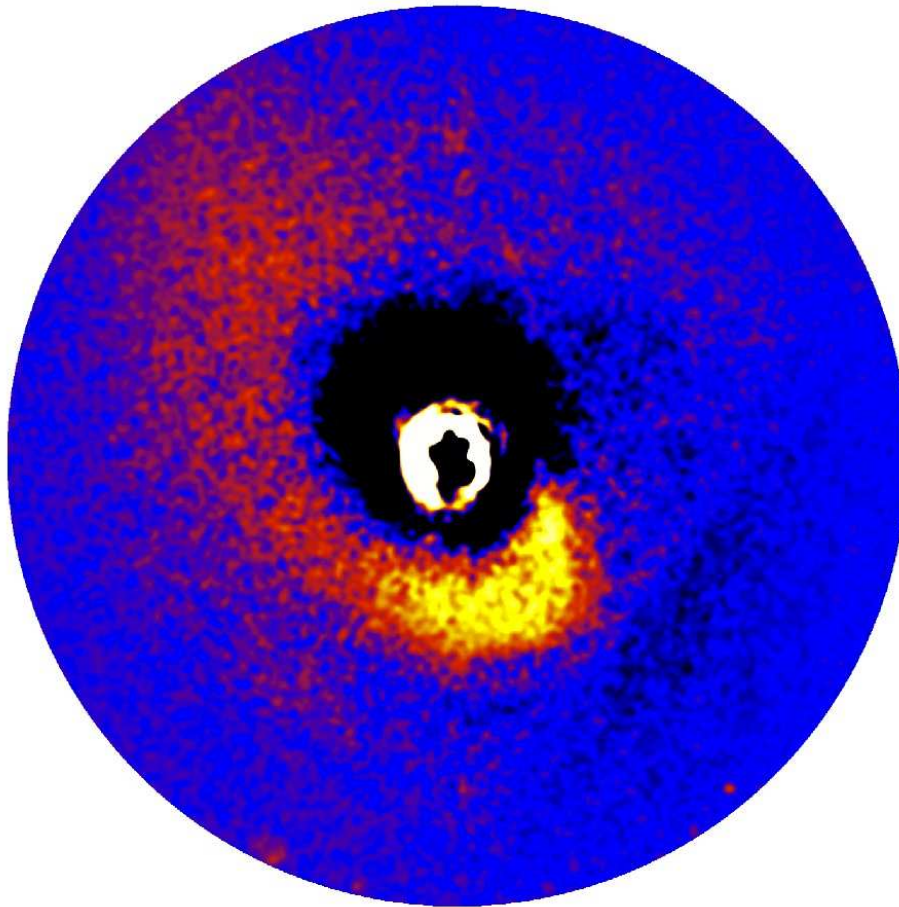


FIG. 7.— Residual image in the $0.3 - 2$ keV band of the central $5''.66$ (240 kpc) radius region of A2052 resulting from the subtraction of a 2D beta model. The image has been smoothed with a $7''.38$ Gaussian. In addition to the bubble rims seen in the center of the image, on larger scales, a spiral is visible extending from the SW to the NE. The linear feature in the SW is a chip-edge artifact.

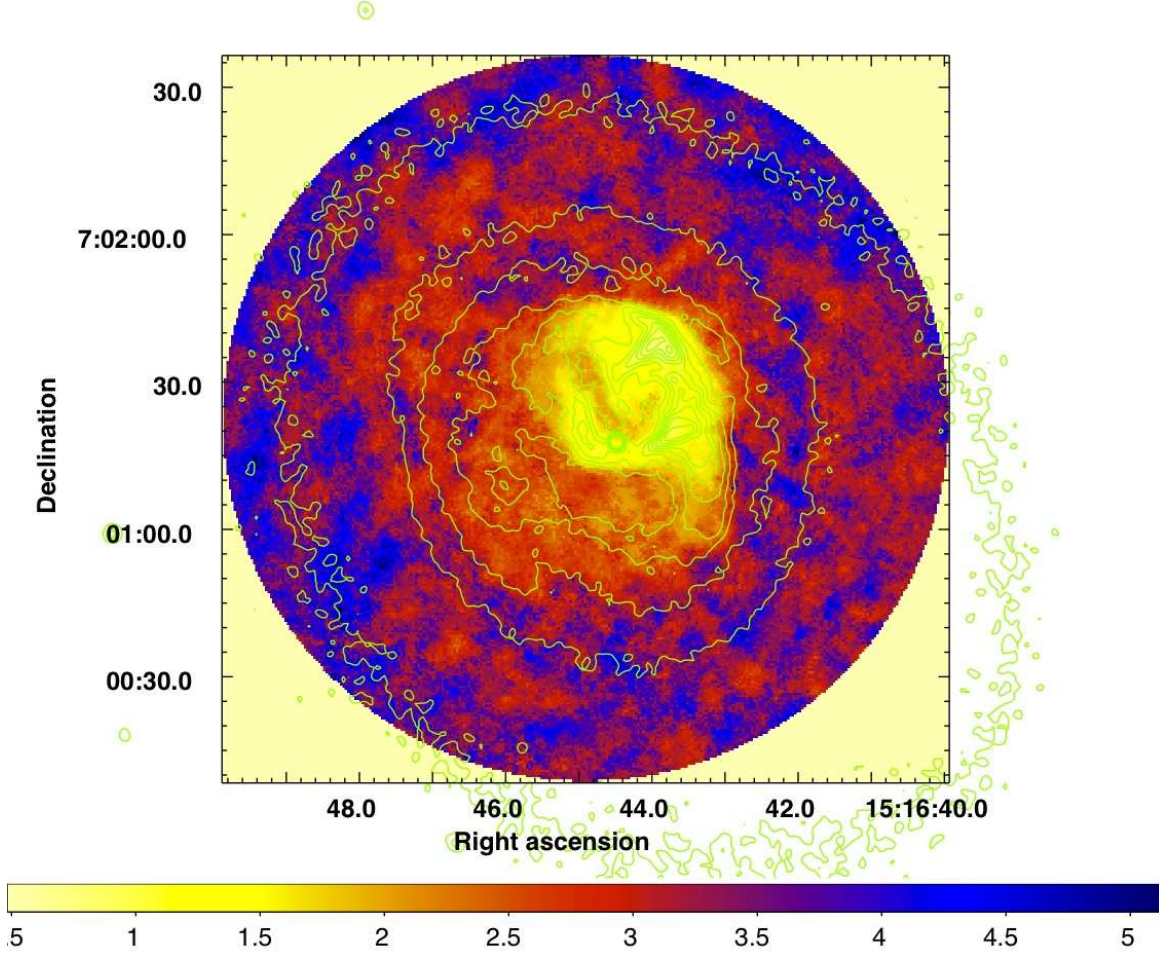


FIG. 8.— High-resolution temperature map of the central region of A2052 with X-ray surface brightness contours in the 0.3 – 10.0 keV range superposed. The scale bar is kT in units of keV. The rims surrounding the X-ray cavities are cool, and the coolest regions, in projection, are coincident with the brightest regions of the rims.

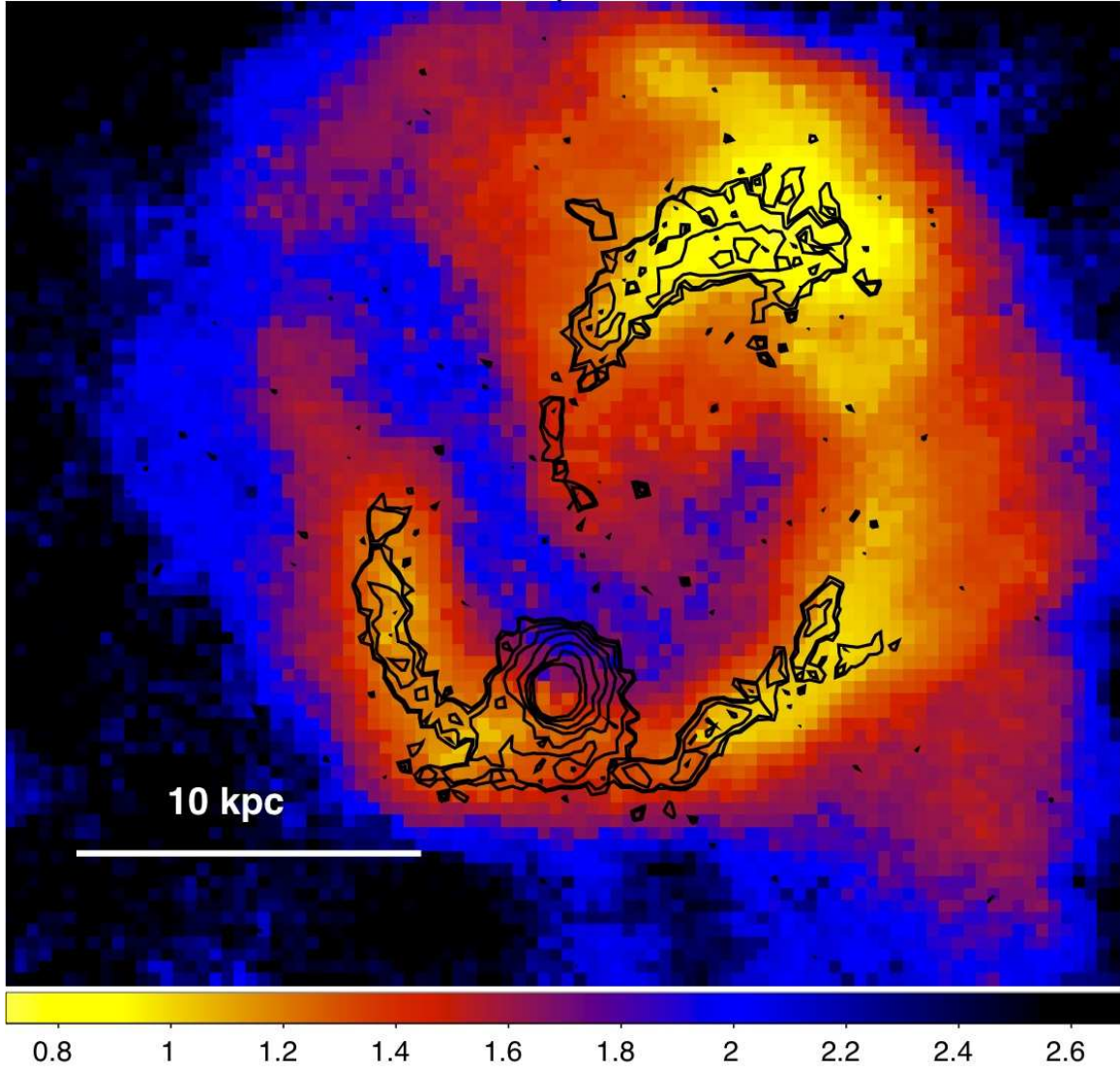


FIG. 9.— $H\alpha$ contours from McDonald et al. (2010) superposed onto the central portion of the high-resolution temperature map from Fig. 8. The coolest regions seen in the X-ray are coincident with emission in $H\alpha$, representing gas with $T \approx 10^4$ K. The scale bar is kT in units of keV.

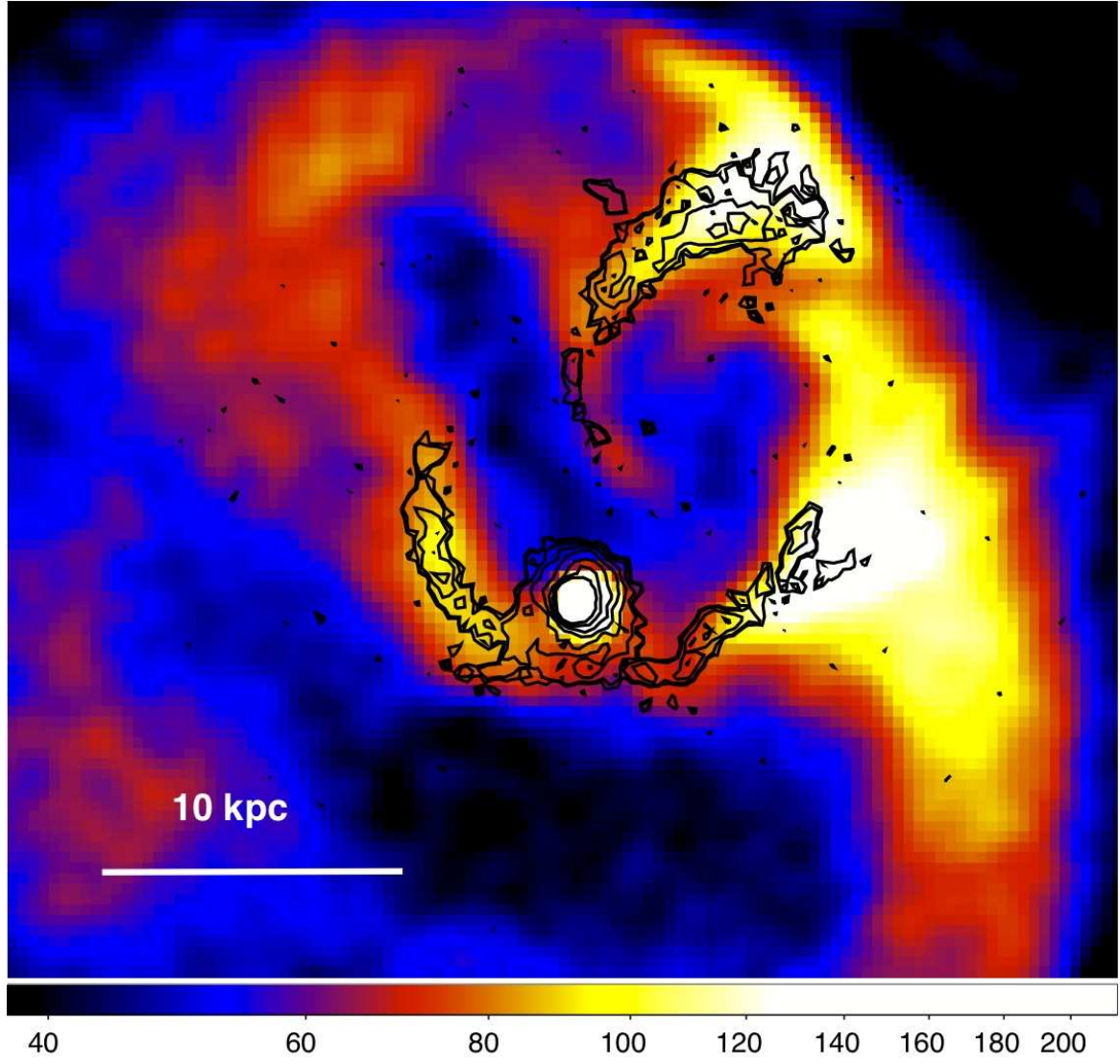


FIG. 10.— *Chandra* image in the 0.3 – 10.0 keV band, smoothed with a 1''.5 radius Gaussian, and superposed with contours of $H\alpha$ emission (McDonald et al. 2010). The X-ray brightest regions in the cluster center show excellent correspondence with the $H\alpha$ emission.

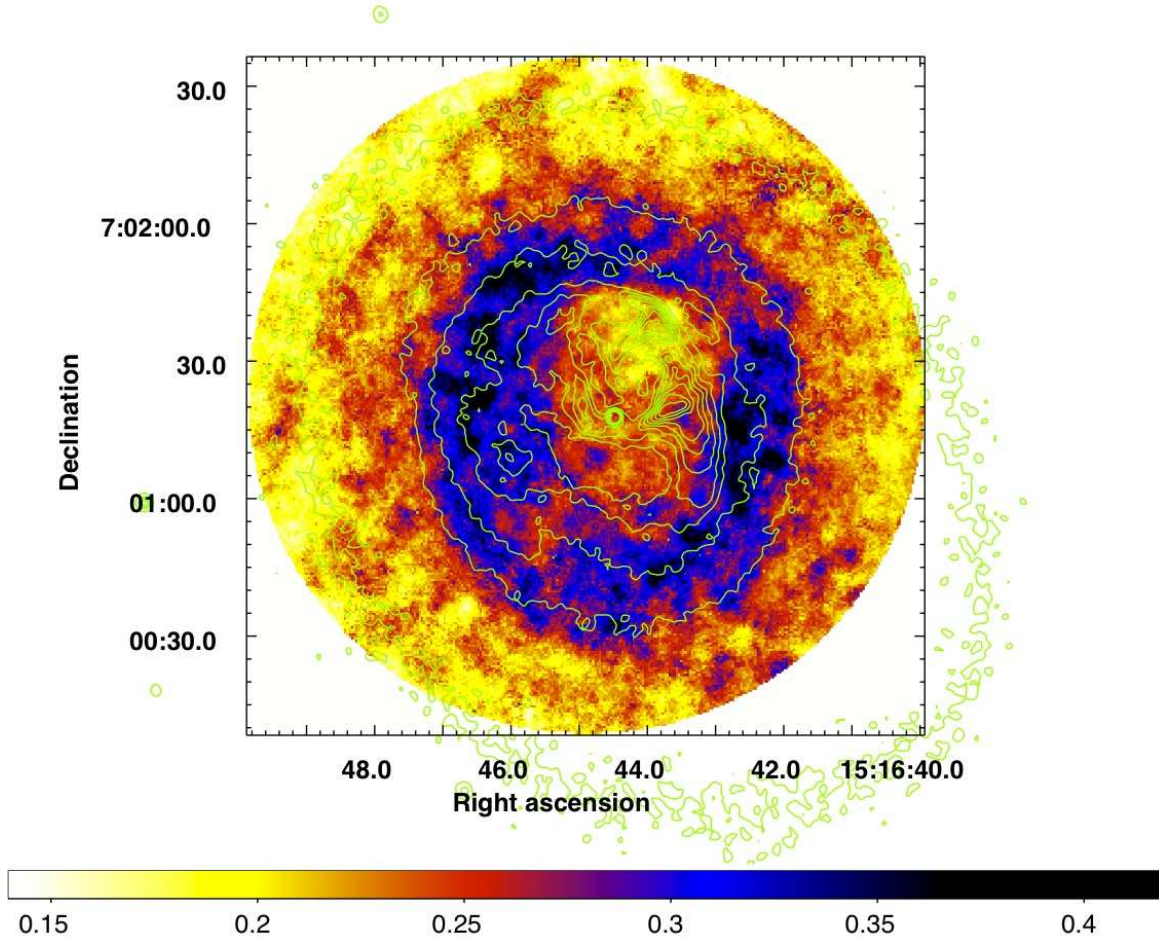


FIG. 11.— Pseudo-pressure map of the central region of A2052 with X-ray surface brightness contours in the 0.3 – 10.0 keV range superposed. A region of high pressure is seen surrounding the cluster center, outside of the bubble rims, and coincident with the inner shock feature.

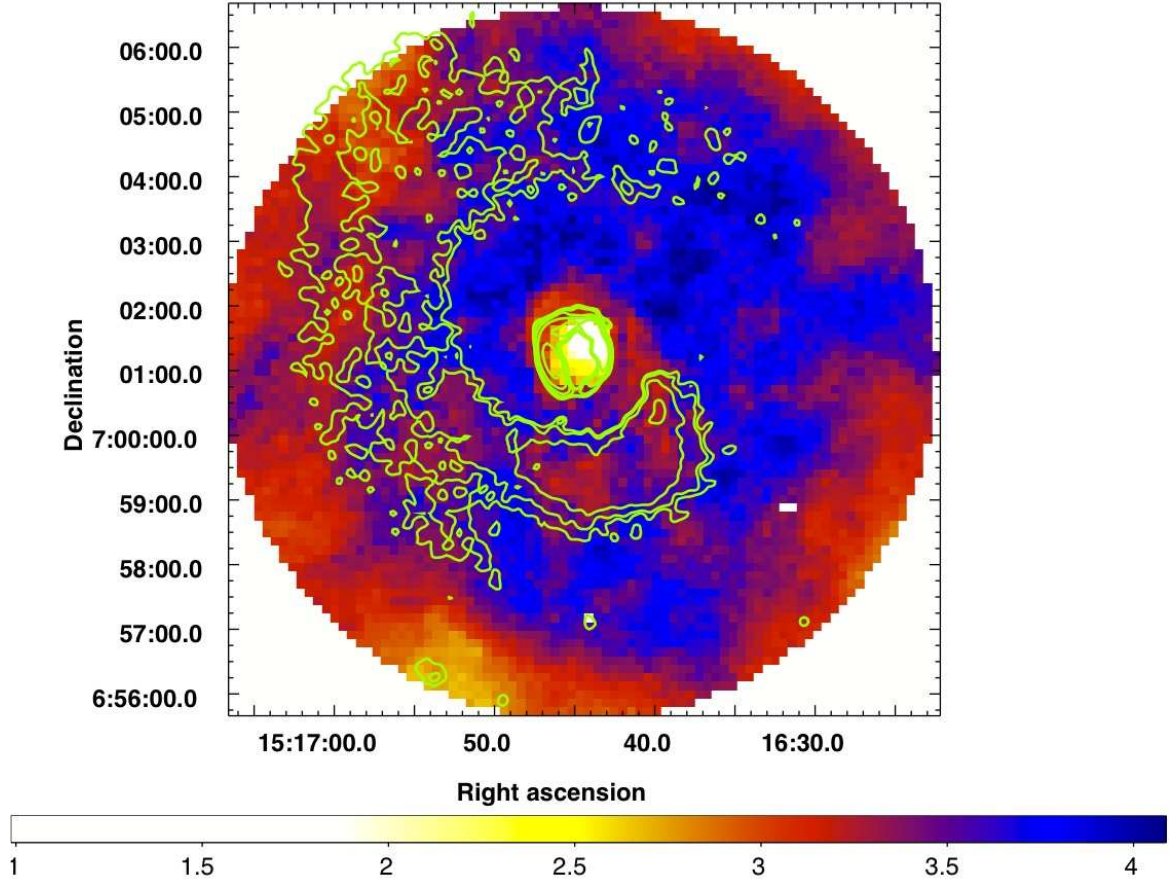


FIG. 12.— Temperature map using a minimum of 10000 background-subtracted counts for each spectral fit. Contours of residual surface brightness showing the spiral feature are superposed. The spiral traces out a region of cooler temperatures. The scale bar is kT in units of keV. Errors range from 1% in the inner regions to 5% in the outskirts of the map. Holes to the far S and SW are excluded point source regions.

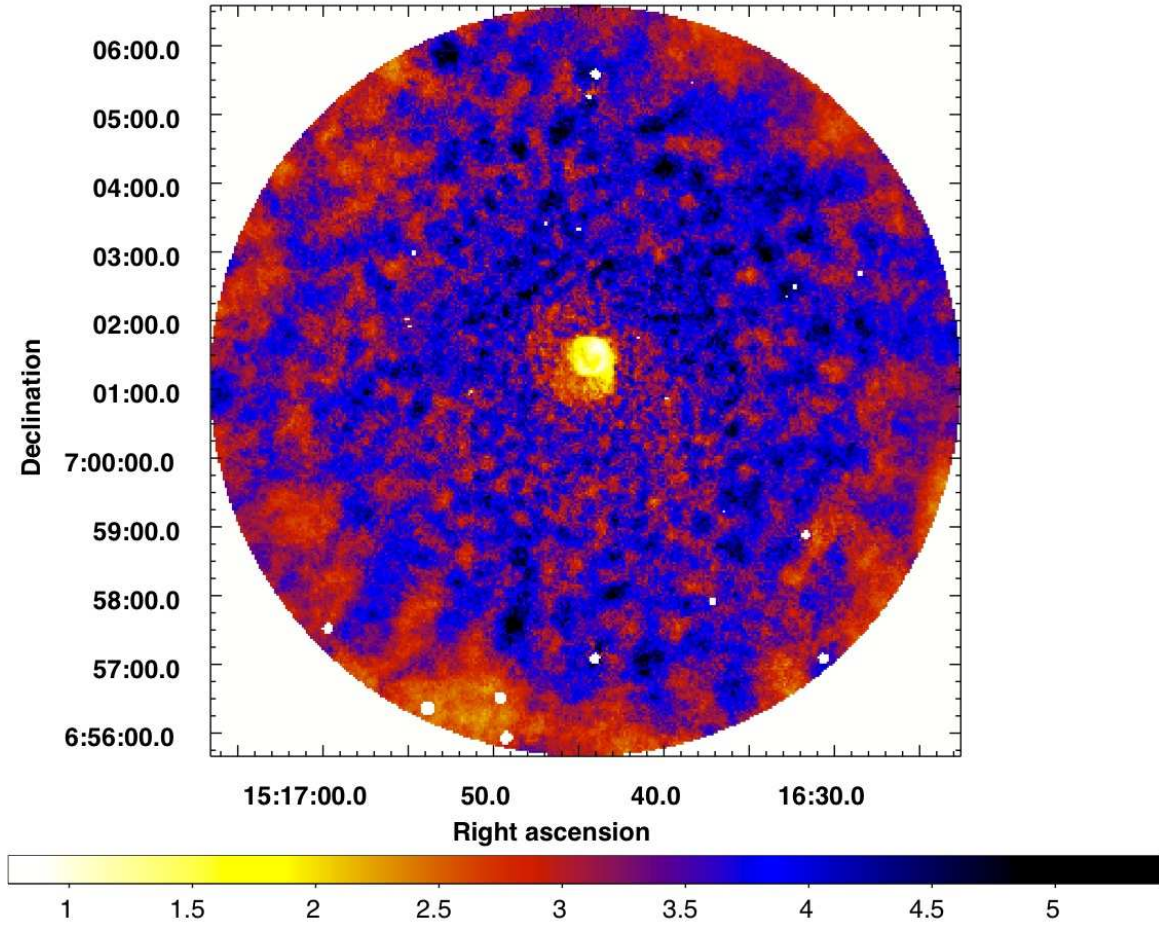


FIG. 13.— Temperature map with the same f.o.v. as Fig. 12, but at higher resolution and using a minimum of 2000 background-subtracted counts for each spectral fit. The map contains results from more than 80000 spectral fits. The scale bar is kT in units of keV. Errors range from 2% in the cluster center to 14% in the outer parts of the frame.

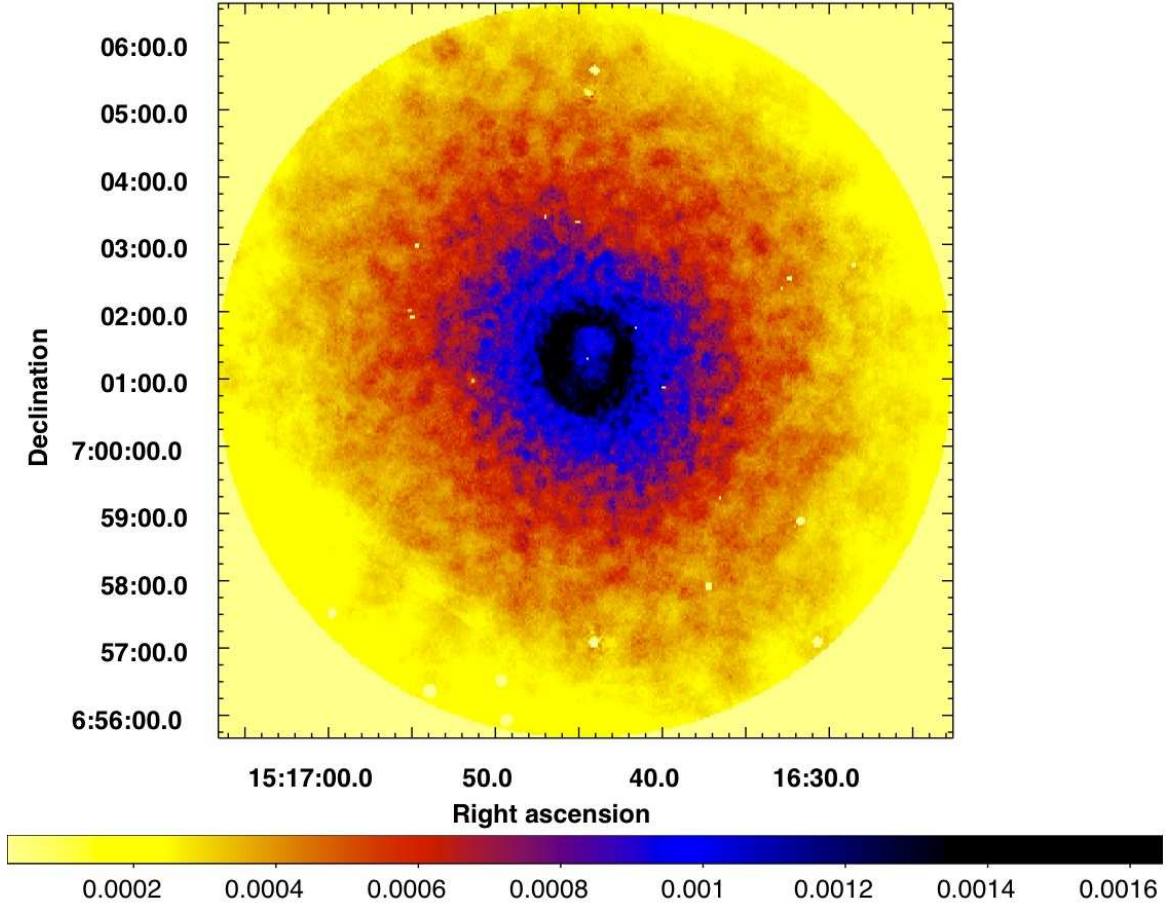


FIG. 14.— Pseudo-pressure map using the spectral fits that resulted in the temperature map in Fig. 13. As in Fig. 11, the slightly N-S elliptical region corresponding to the inner shock is seen. There is no evidence for a region of pressure that corresponds with the spiral feature seen in Fig. 7.

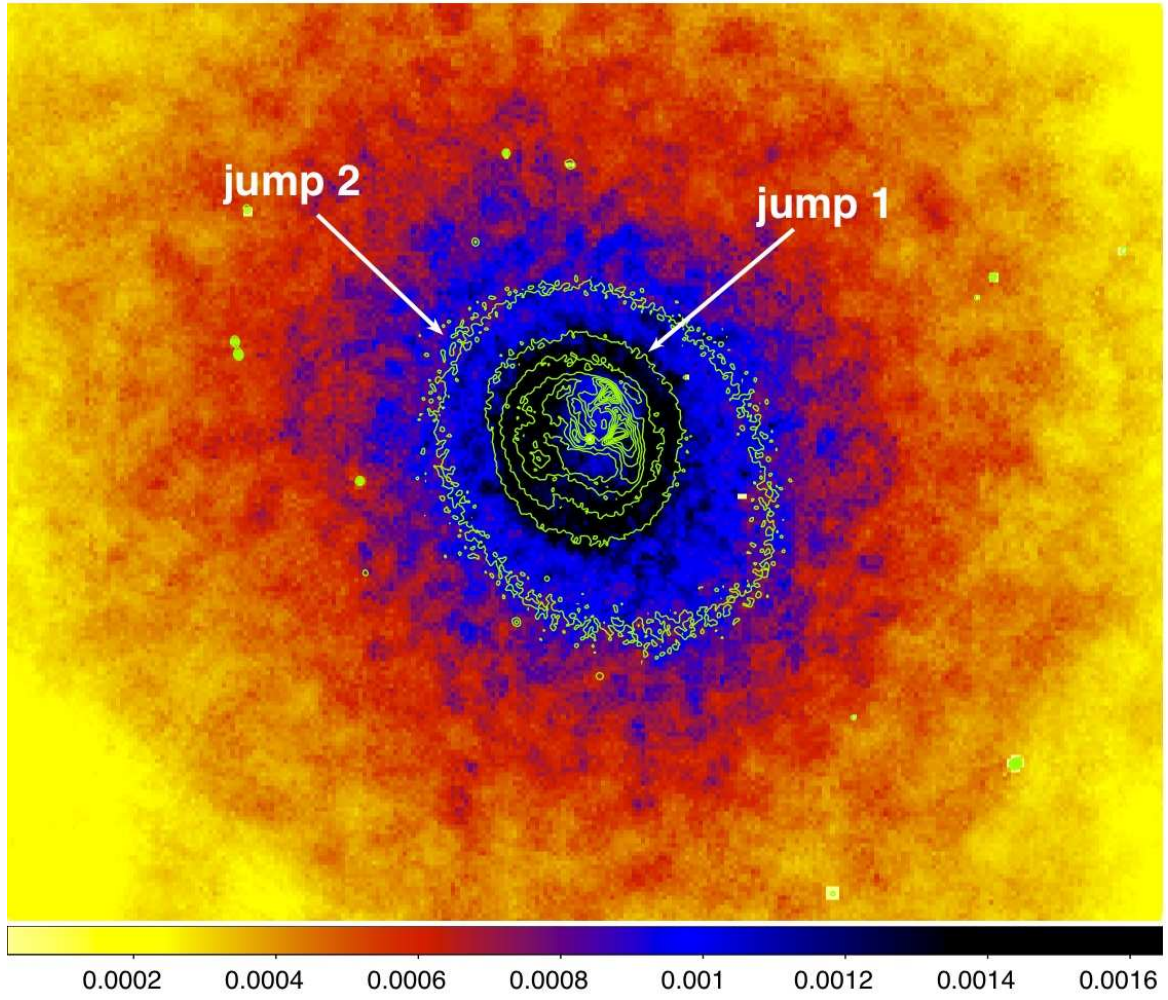


FIG. 15.— Zoomed-in view of the pseudo-pressure map shown in Fig. 14 with X-ray surface brightness contours superposed. The first inner jump in surface brightness traces out a jump in pressure, and the second inner surface brightness jump traces out a region of enhanced pressure.

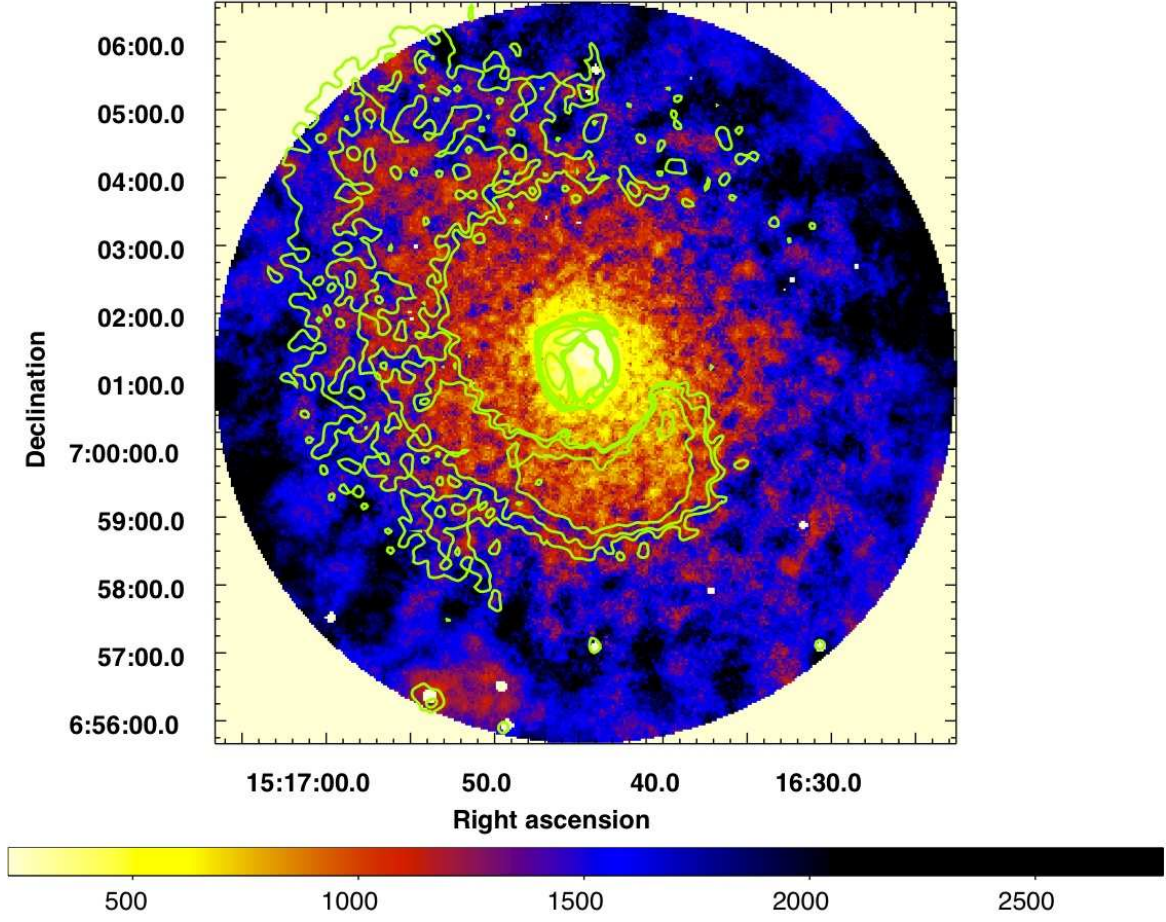


FIG. 16.— Pseudo-entropy map with excess surface brightness contours (after 2D beta model subtraction) superposed. There is an overall decrease in entropy towards the cluster center and the spiral feature is coincident with low entropy structure in the map.

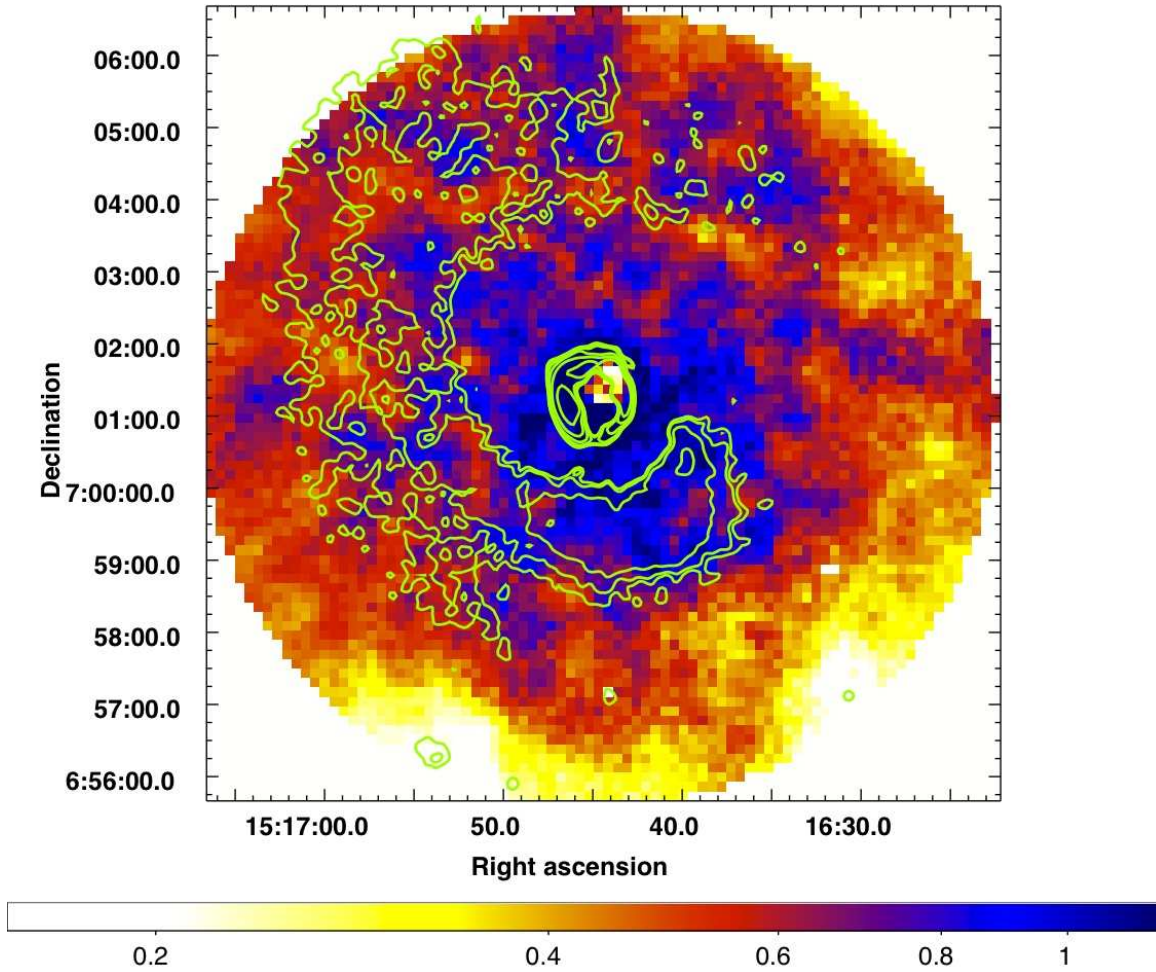


FIG. 17.— Projected abundance map with contours of the spiral excess superposed. A region of high metallicity is coincident with the SW portion of the spiral. Abundances shown are relative to solar. The region of apparent high abundance in the NW bubble rim is at least partly the result of fitting a one-temperature model to the projected multi-temperature gas in this area. Errors range from 5% in the inner regions to 23% in the outskirts of the frame, with the majority of the errors at the 10 – 15% level across the map.

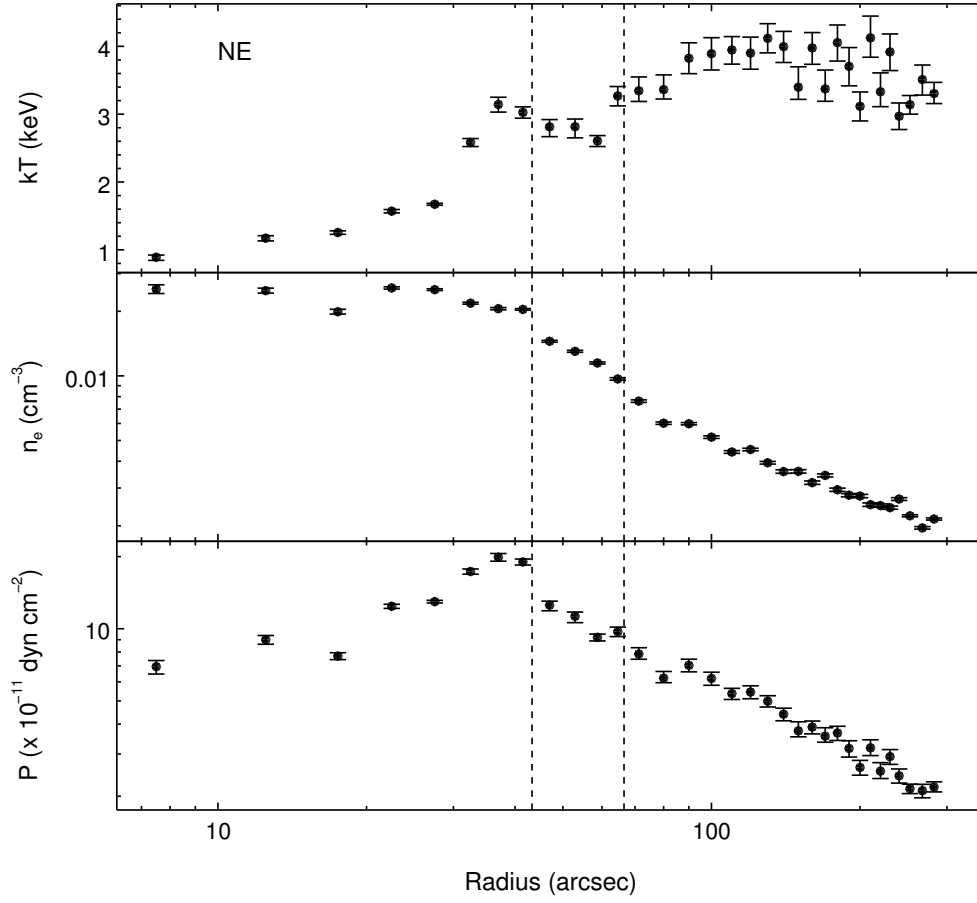


FIG. 18.— Deprojected temperature profile, and profiles of density and pressure for the NE sector. Positions of the inner shocks are marked with dashed lines. A clear rise in temperature and pressure is seen inside the innermost shock.

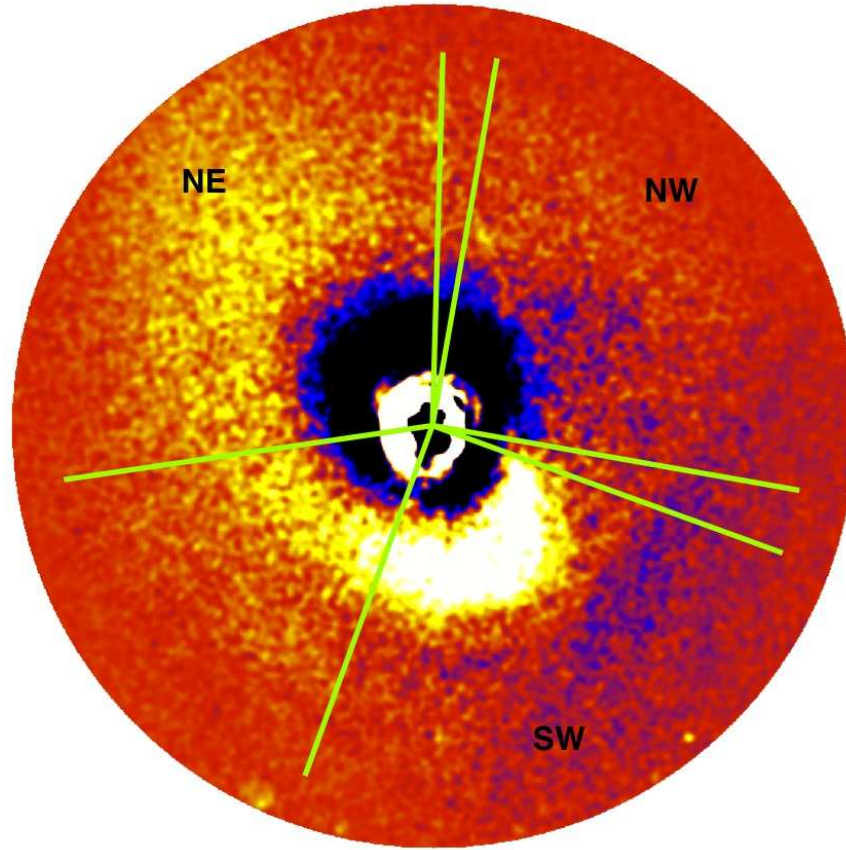


FIG. 19.— Residual image in the $0.3 - 2$ keV band of the central $5''.66$ (240 kpc) radius region of A2052 resulting from the subtraction of a 2D beta model and smoothed with a $7''.38$ Gaussian. Superposed on the image are the SW, NE, and NW sectors from which the surface brightness and temperature profiles shown in Figs. 18, 20, 21, 22, and 23 were extracted.

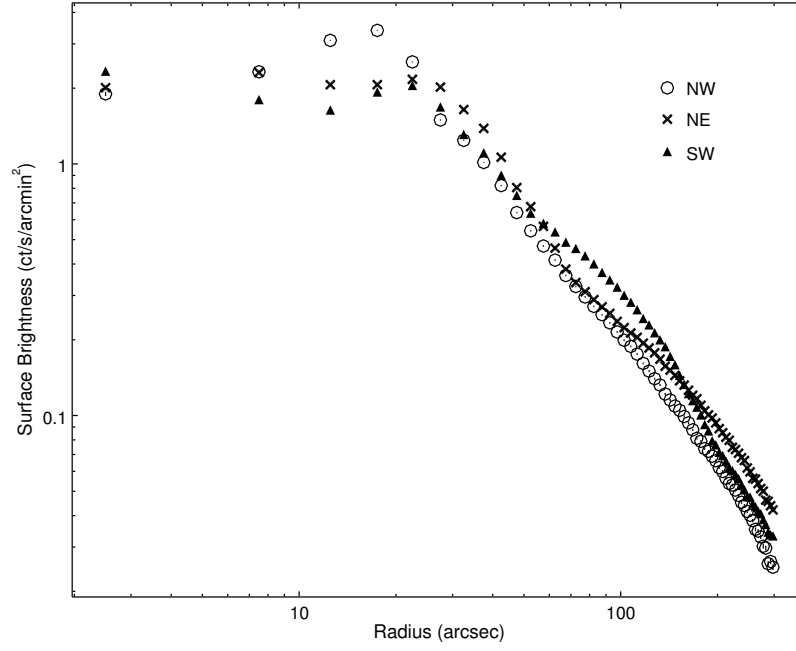


FIG. 20.— Surface brightness profiles in the 0.3 – 10 keV band corresponding to the sectors shown in Fig. 19. Clear excesses are seen in the regions of surface brightness enhancement associated with the spiral feature in Figs. 7 and 19. For the SW, the excess extends from $\approx 60'' - 195''$, while for the NE, the excess is seen at radii beyond $\approx 110''$.

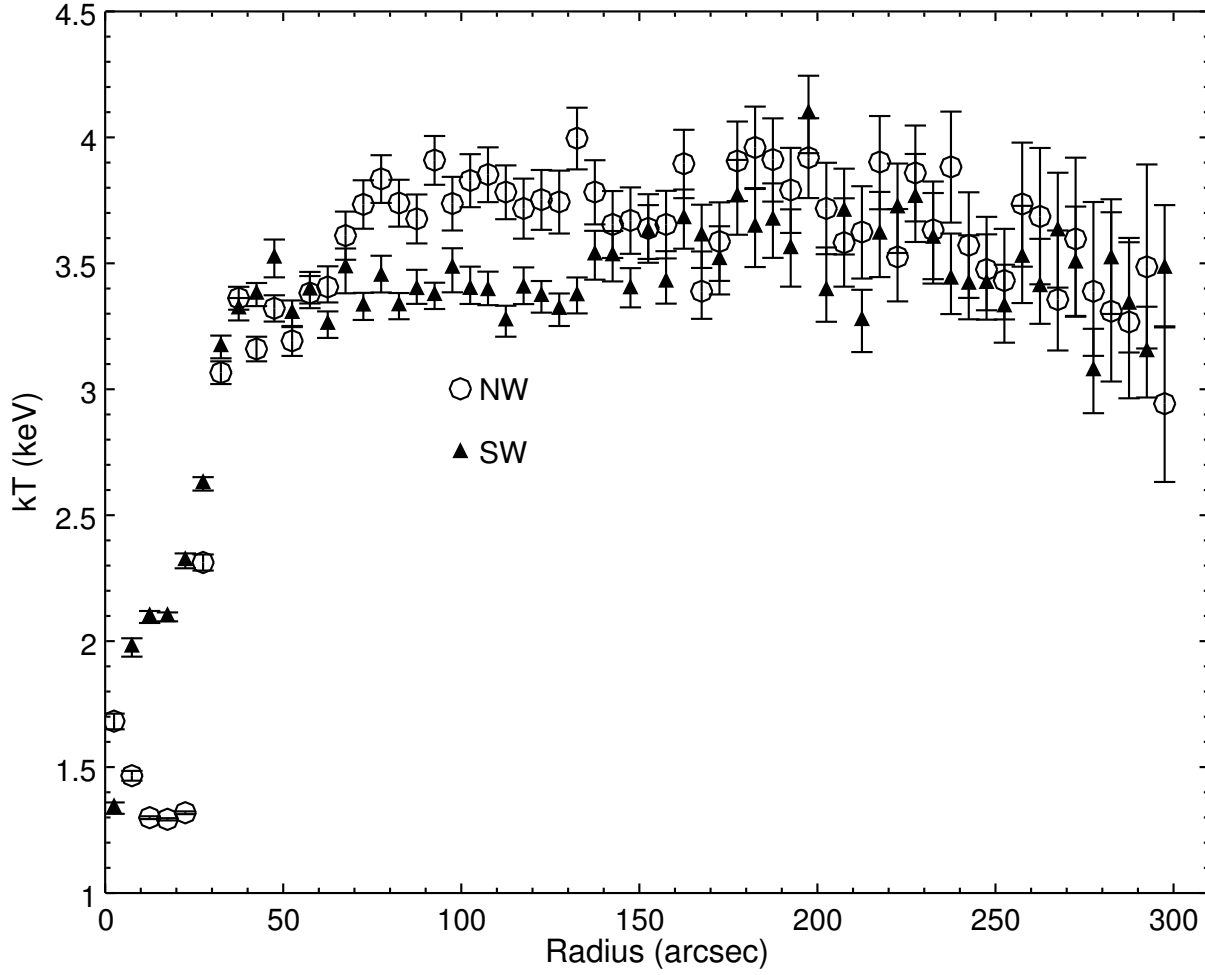


FIG. 21.— Projected temperature profiles for the SW and NW sectors shown in Fig. 19. The SW sector corresponds with the bright, inner, spiral region, while the NW sector is the non-spiral, comparison region. The SW spiral excess corresponds with regions of cooler temperature in the radial range $\approx 60'' - 140''$. The profiles converge beyond $\approx 140''$.

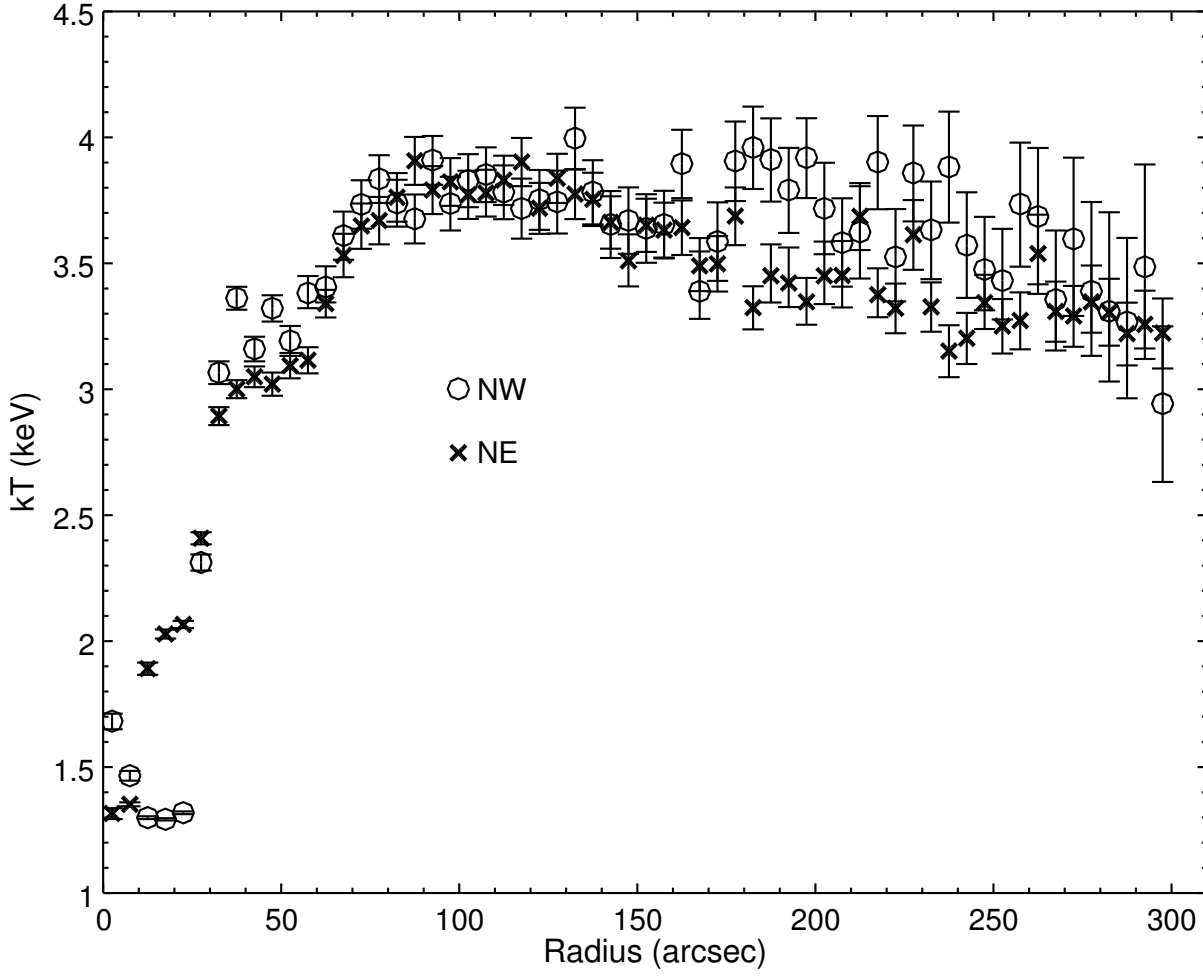


FIG. 22.— Projected temperature profiles for the NE and NW sectors shown in Fig. 19. The NE sector corresponds with the outer spiral region, while the NW sector is the non-spiral, comparison region. Cooler temperatures are seen associated with the NE spiral excess (radii $> 160''$).

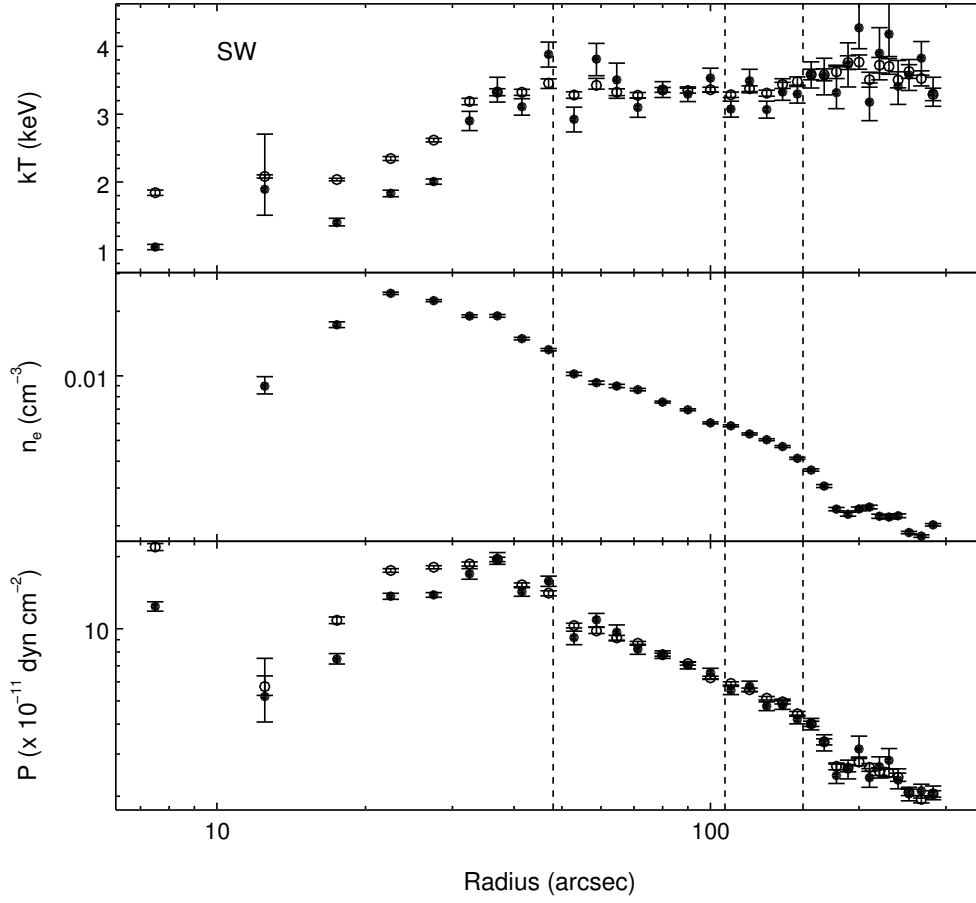


FIG. 23.— Profiles of temperature, density, and pressure in the SW sector. Filled circles indicate results from deprojected fits. The open circles show the projected temperature profile and the pressure profile derived using the density and the projected temperatures. Dashed lines show the positions of the first inner shock, the second inner shock / edge, and the cold front / SW spiral edge, going from smaller to larger radii.

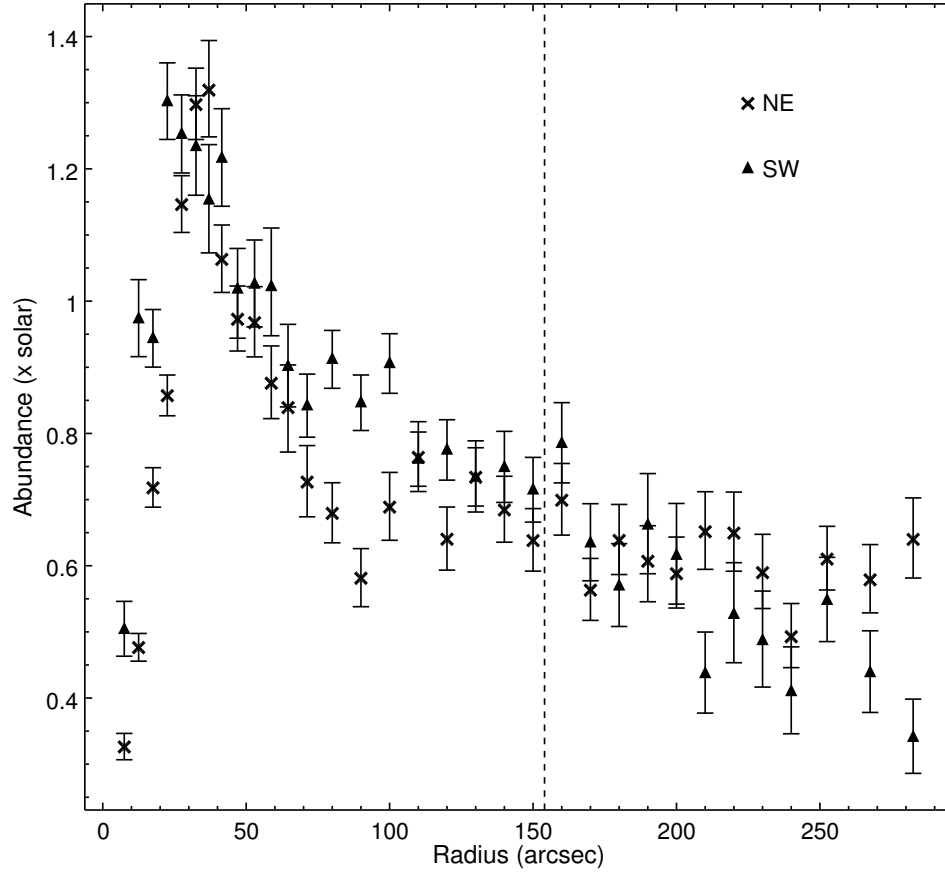


FIG. 24.— Projected abundance profiles for the SW and NE regions. The dashed line indicates the outer edge of the SW spiral / cold front. The abundances are higher inside the SW spiral region (from $\approx 70'' - 120''$) compared to the corresponding radial region to the NE.

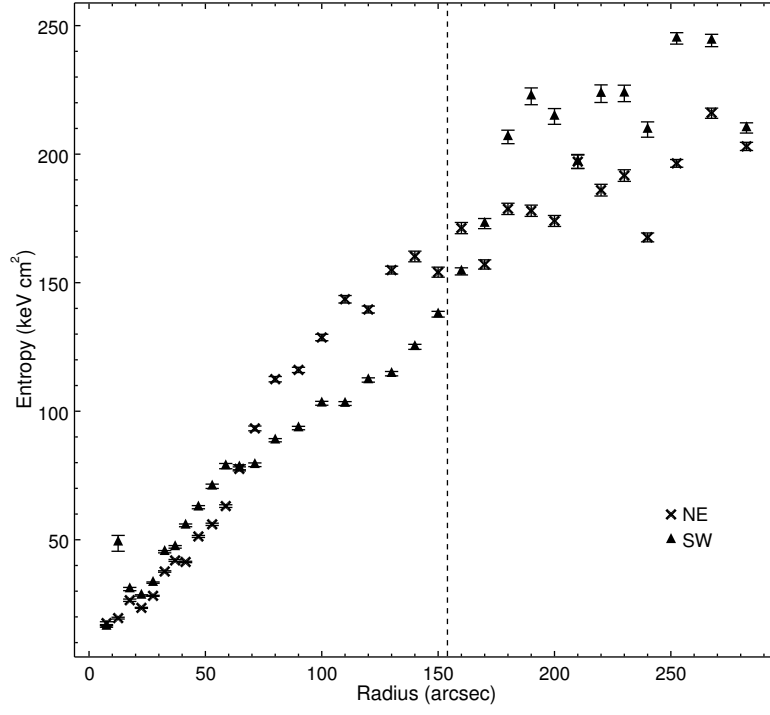


FIG. 25.— Entropy profiles for the SW and NE regions with entropy defined as $S = kT/n_e^{2/3}$, and using projected temperatures. The dashed line indicates the outer edge of the SW spiral. The spiral surface-brightness excess is very well traced by the entropy structure. The spiral excess to the SW ($r \approx 70 - 150''$) corresponds with a region of lower entropy. At larger radii $r > 190''$, the spiral excess in the NE also is shown to have lower entropy values as compared to the non-spiral region in the SW at these large radii.

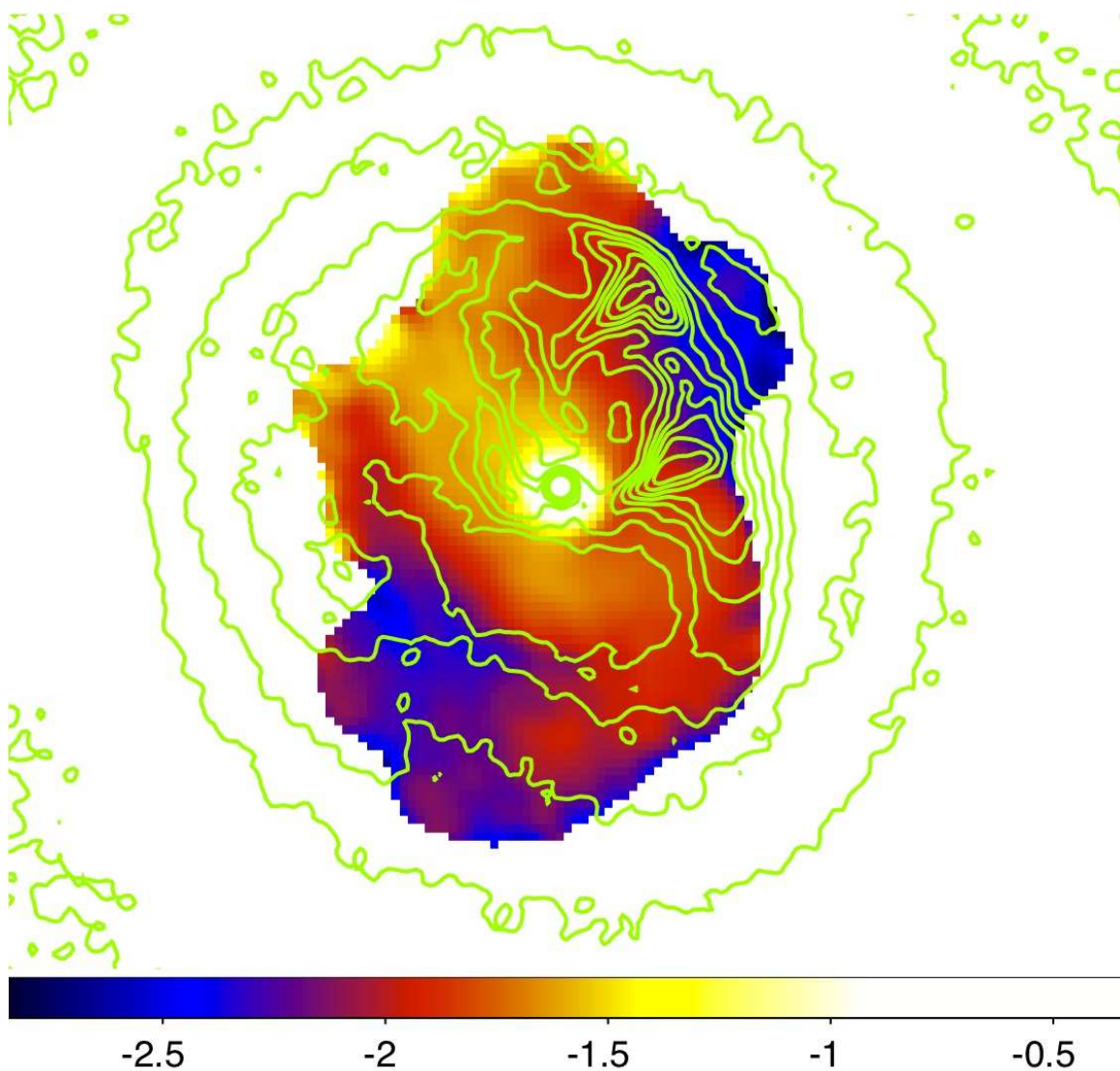


FIG. 26.— Radio spectral index map created using the 1.4 and 4.8 GHz data. Contours of 0.3 – 10.0 keV X-ray surface brightness are superposed. The outer bubbles to the NW and SE are filled with radio emission with steeper spectral index, consistent with these regions being inflated by an earlier outburst of the AGN.

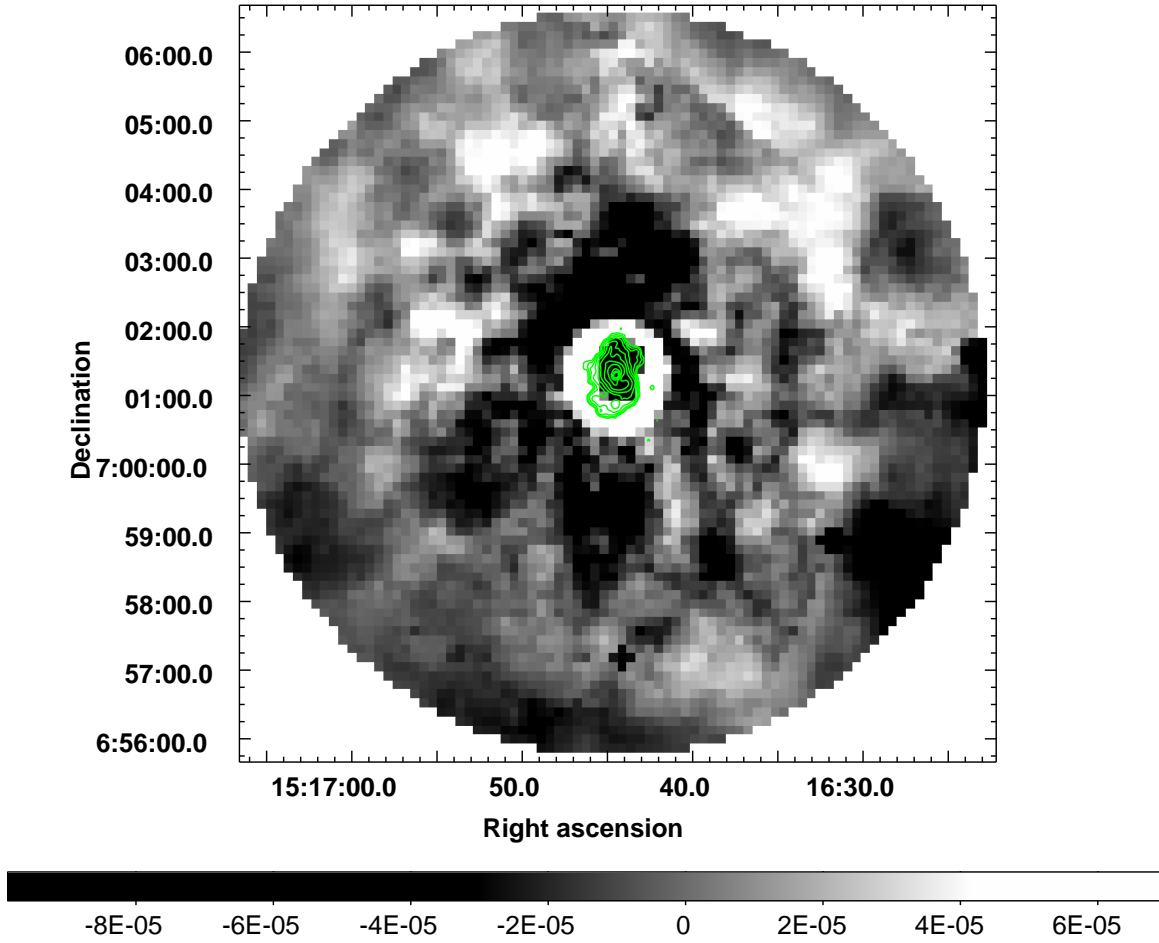


FIG. 27.— Pressure residual map created by subtracting off a 2D beta model fitted to a pseudo-pressure map with 4.8 GHz radio contours superposed. The inner shock is seen as a pressure enhancement exterior to the radio lobes. In addition, large deficits in pressure are seen to the N and S of the cluster center. These may represent “ghost cavities” related to an earlier AGN outburst.